

Static and quasi-elastic small angle neutron scattering on biocompatible ionic ferrofluids: magnetic and hydrodynamic interactions

F Gazeau¹, F Boué², E Dubois³ and R Perzynski^{1,4}

¹ Laboratoire des Milieux Désordonnés et Hétérogènes—UPMC Case 78, 4, Place Jussieu, 75252 Paris Cedex 05, France

² Laboratoire Léon Brillouin, CEA CNRS UMR 12, CE Saclay, 91191 Gif-sur-Yvette, France

³ Laboratoire des Liquides Ioniques et Interfaces Chargées, UPMC Case 63, 4, Place Jussieu, 75252 Paris Cedex 05, France

E-mail: rperz@ccr.jussieu.fr

Received 16 October 2002, in final form 11 December 2002

Published 7 April 2003

Online at stacks.iop.org/JPhysCM/15/S1305

Abstract

We investigate the structure and dynamics of ionic magnetic fluids (MFs), based on ferrite nanoparticles, dispersed at $\text{pH} \approx 7$ either in H_2O or in D_2O . Polarized and non-polarized static small angle neutron scattering (SANS) experiments in zero magnetic field allow us to study both the magnetic and the nuclear contributions to the neutron scattering. The magnetic interparticle attraction is probed separately from the global thermodynamic repulsion and compares well to direct magnetic susceptibility measurements. The magnetic interparticle correlation is in these fluid samples independent of the probed spatial scale. In contrast, a spatial dependence of the interparticle correlation is evidenced at large Φ by the nuclear structure factor. A model of magnetic interaction quantitatively explains the under-field anisotropy of the SANS nuclear contribution.

In a quasi-elastic neutron spin-echo experiment, we probe the Brownian dynamics of translation of the nanoparticles in the range $1.3 \leq q R_g^N \leq 10$ (q , scattering vector; R_g^N , nuclear radius of gyration of the nanoparticles). For the first time in an MF, we determine the hydrodynamic function at large q vectors.

1. Introduction

The development of biocompatible ionic ferrofluids has recently opened attractive and promising prospects in biophysics and medicine. For example, eucaryotic living cells are able to internalize the magnetic nanoparticles used in the present work by endocytosis [1, 2].

⁴ Author to whom any correspondence should be addressed.

The process strongly concentrates the nanoparticles in intracytoplasmic organelles. Those magnetic endosomes are micron-sized magnetic vesicles that can be visualized by optical microscopy. Such a cell magnetic labelling is used *in vivo* to track targeted cells by magnetic resonance imaging [3, 4]. Another application *in vitro* is to use those magnetic endosomes as local probes of the intracellular rheology following their individual deformation under an applied field [5]. A concentrated magnetic fluid (MF) is trapped inside the endosomes. The details of the magnetic and hydrodynamic interparticle interactions in the MF are of paramount importance to understand its magneto-rheological behaviour at the colloidal scale. The knowledge of the structural and dynamic properties is also a current goal to explain more macroscopic spectacular and sometimes unexpected MF behaviours [6–13]. In those materials [14–16], the specific coupling between magnetic and hydrodynamic degrees of rotation allows for original magneto-rheological applications such as assisted clutches or dampers [14, 17].

With the long range prospect of these biological applications, a well defined system has been developed [18–20]. It is based on ferrite nanoparticles stabilized in aqueous media at $\text{pH} \approx 7$ by a citrate coating of the particles. The colloidal phase diagram of the system has already been studied in detail [21–24]. It presents a gas–liquid-like phase transition [21] with an associated critical point [22, 23]. For an osmotic pressure larger than that of the critical conditions, fluid and glassy solid phases can be obtained. Here, we address ourselves to a detailed probing of the MF interparticle interactions in the fluid phase. There, the global thermodynamic interaction is repulsive and the magnetic interaction is experimentally known to be unable to lead to an interparticle contact chaining or to a colloidal phase separation, even under a saturating field [25].

Small angle neutron scattering (SANS) is the most powerful technique available to elucidate the colloidal structure and the interparticle interactions in an MF at scales spreading from 5 up to 100 nm. On their side, x-rays and light scattering are highly penalized by the strong absorption of MF in their wavelength domains. In a previous work [25], using a static non-polarized SANS device, we obtained part of the effects. However, among the global thermodynamic interactions, we were not able to weight specifically the magnetic interparticle interaction. For that purpose a polarized device is necessary. The hydrodynamic interparticle interaction being also relevant to our problem, we also need to develop a dynamical experiment. A neutron spin-echo (NSE) spectrometer allows for those two kinds of measurement.

We present here two different experiments performed on the MESS spectrometer at Orphée-LLB-Saclay-France:

- a static polarization analysis and
- a quasi-elastic NSE experiment.

Complementary non-polarized measurements are performed on PAXY and PAXE in zero-field and under a 68 kA m^{-1} applied field.

In this paper we first present in section 2 the current state of the art on static and quasi-elastic SANS. We introduce in section 3 the characteristics of the MF samples tested here, discussing their colloidal stability and their magnetic properties. After this we divide the paper into two distinct parts, section 4 for the statics and section 5 for the dynamics. In section 4, after a theoretical background presenting the nuclear and the magnetic contributions to SANS, we introduce our experimental static techniques and discuss our results. In particular, the magnetic scattering is compared to initial magnetic susceptibility measurements. This allows us to sort out the contribution of the dipolar magnetic interaction among the global thermodynamic interparticle interactions. The anisotropic pattern, associated with the under-field nuclear contribution, is then analysed in terms of anisotropic under-field magnetic

interaction. Section 5 presents the quasi-elastic experiment. It probes the Brownian dynamics of translation of the nanoparticles. This process has been previously studied in a similar MF at a much larger spatial scale in a forced Rayleigh scattering experiment [26, 27]. We focus here on the behaviour of the hydrodynamic function at large scattering vector.

2. Current state of the art

There can be two contributions to the neutron scattering, due to the two interactions between a neutron and a nucleus, corresponding to the two contributions to scattering cross-section [28–34].

- *A neutron/nucleus interaction involving nuclear forces leading to the so-called nuclear contribution.* For magnetic nanoparticles dispersed in light water, the scattering length density contrast (see definition below) between the nanoparticles and the water is large. Thus the nuclear contribution dominates and is easy to measure [20–25]. It leads to structural and dynamical determinations which are similar to those extracted from static and quasi-elastic small angle x-ray scattering [35–40] or, at different spatial scales, from static and quasi-elastic light scattering [41, 42].
- *A neutron-spin/nucleus-spin interaction, leading to the so-called magnetic scattering.* The nucleus spins, if they are important, interact with the local magnetization inside the nanoparticles and therefore with the nanoparticle magnetic moment (nanoparticle spin). This leads to structural and dynamical magnetic information. It is an important specificity of SANS. In the static limit of zero scattering vectors a magnetic scattering measurement reduces to a magnetic susceptibility determination. A few static measurements of this magnetic scattering contribution in MF have been performed [29, 32–34, 43–45]. However they scarcely cover the concentrated regime that interests us here. As well, a very few dynamic measurements of the magnetic scattering contribution have been performed [46, 47].

Both nuclear and magnetic contributions can be present in static and quasi-elastic SANS experiments [29, 44, 45, 47].

- In a static experiment, the nuclear contribution is sensitive to all the thermodynamical interactions present inside the colloidal solution [20, 21, 25]. In a quasi-elastic experiment, the nuclear contribution is sensitive to all the thermodynamical interactions *and also* the hydrodynamical interaction.
- In both static and dynamic experiments, the magnetic contribution specifically sorts out the magnetic dipolar interaction. Note however that in a dynamic experiment the magnetic dynamics is highly complicated by the internal magnetodynamics of the magnetic grains [46, 47].

The neutron intensity scattered by an MF in a small angle experiment can be rather variegated and miscellaneous. The following are examples.

- It is possible to obtain anisotropic patterns under field whereas the nuclear and the magnetic structure factors remain isotropic [45] if the magnetic contribution is important.
- It is possible to obtain anisotropic patterns under field even though the magnetic contribution of the neutron scattering is negligible (see figure 10 further on and [25]), if the magnetic interaction contributes substantially to the interparticle interaction. The nuclear contribution is sensitive to all the thermodynamic interactions including the dipolar magnetic one.

- In our ionic MF, the nuclear neutron scattered pattern may well depend strongly on temperature (in the range 10–35 °C) [21, 22] whereas it can also be totally insensitive to it (in the same range of T) [19]. It depends on the thermodynamical state of the sample and on the distance of this state from the critical point [22] associated with the gas–liquid transition.

The interparticle interaction is thus clearly of importance for the shape adopted by the neutron scattering pattern. The difficulty is that in a standard SANS experiment on an MF, nuclear and magnetic contributions are mixed. For a detailed analysis, it is necessary to separate them.

Methods of nuclear index matching [48], which tune the density of nuclear diffusion length of the solvent with respect to that of the nanoparticles in order to suppress the nuclear contrast, and hence their nuclear signal, are rather difficult to undertake and not always efficient. Firstly the scattering length density of the nanoparticles is usually above the range covered by mixtures of solvents, deuterated and non-deuterated. Secondly the nanoparticle surface is frequently coated with chemical species in order to ensure their colloidal stability. The nuclear contribution coming from this surface coating becomes important in those contrast variation experiments. It complicates the analysis, introducing an extra contribution of the same order of magnitude as the two previous ones.

Another method proposed by [29] is an under-field experiment. If the magnetic nanoparticles are fully aligned by the field, the magnetic signal is null along the field and maximal in the perpendicular direction. Such a method is only efficient if the magnetic contribution is large enough with respect to the nuclear one and does not permit a study of the magnetic interactions in zero fields. Moreover, in intermediate fields, the moment alignment is not complete and in that case also the analysis is difficult.

We have chosen here another route [32–34]. The nuclear and the magnetic scattered contributions depend on the direction of the neutron polarization. It is possible to take advantage of those properties to separate the two contributions by a polarization analysis [32–34, 49]. This will be detailed in section 4.1.2.

3. Samples

3.1. Chemical synthesis

The MFs used here are chemically synthesized after Massart's method [20, 50, 51]. They are colloidal suspensions of ferrite particles (here either cobalt ferrite CoFe_2O_4 or maghaemite $\gamma\text{-Fe}_2\text{O}_3$) in an aqueous medium. The nanoparticles are obtained by coprecipitation in an alkaline medium of an aqueous mixture of divalent metal M^{2+} (either Co^{2+} or Fe^{2+}) and Fe^{3+} salts. The synthesized particles, of mean size ranging from 3 to 20 nm [17], are macro-anions coated with hydroxo ligands ($-\text{OH}$). Thanks to the acido-basic properties of their surfaces, the particles can be dispersed either in strongly alkaline ($\text{pH} \geq 12$) or strongly acidic aqueous media ($\text{pH} \leq 2$). The point of zero charge (PZC) is 7.5 and does not allow dispersion of the particles at $\text{pH} = 7$. To obtain aqueous dispersions at $\text{pH} = 7$, as required for biological applications, the PZC is shifted down to $\text{pH} = 2$ by coating the particle surface with citrate ligands. The surface charge is negative and depends on the concentration of citrate molecules inside the solution because there is equilibrium between adsorbed and free molecules. The charge reaches a saturation value for high enough citrate concentrations: 2 charges nm^{-2} for the $\gamma\text{-Fe}_2\text{O}_3$ nanoparticles and 1.6 charges nm^{-2} for the CoFe_2O_4 ones [20, 25]. The samples studied here always lie in this saturated regime. The volume fraction Φ of the obtained solutions is determined by chemical titration of iron. It ranges here from 5 to 20%. As we fix roughly

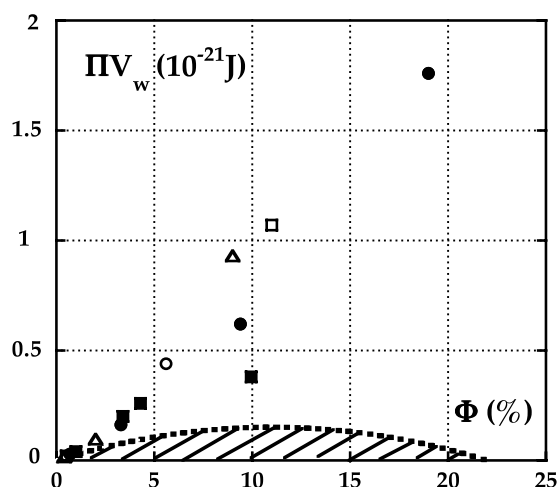


Figure 1. Localization of the various samples of table 1 on the phase diagram of the colloidal system. Π , osmotic pressure; V_w , weight averaged volume of the nanoparticles; Φ , nanoparticle volume fraction. Dotted curve: experimental liquid–gas coexistence curve limiting the diphasic (hatched) area of the phase diagram. Symbols: (■) samples A; (●) samples B; (□) samples C; (Δ) samples D and (○) samples E.

$[\text{cit}]_{\text{free}} \approx 0.5\Phi \text{ mol l}^{-1}$, here $[\text{cit}]_{\text{free}}$ varies from $2.5 \times 10^{-3} \text{ mol l}^{-1}$ at $\Phi = 0.5\%$ up to $\approx 0.1 \text{ mol l}^{-1}$ at Φ of the order of 20%. The samples are all dispersed in light water except one sample in D_2O (sample A0 of table 1). In that case, the citrate-coated particles are synthesized in light water. They are then precipitated in acetone and re-dispersed in heavy water. All the experiments are here performed at room temperature.

3.2. Colloidal stability

Because of the large value of the superficial density of charges Σ associated with a low enough ionic strength, the interparticle electrostatic repulsion is strong. In particular it is strong enough to prevent any flocculation or any gas–liquid phase separation under the van der Waals attractions and the magnetic dipolar interaction. Recently a phase diagram (ΠV_w versus Φ — Π being the osmotic pressure of the solution and V_w the weight average volume of the nanoparticles) has been built up in zero magnetic field for citrated $\gamma\text{-Fe}_2\text{O}_3$ nanoparticles dispersed in water with a saturated density of charge Σ [21–25, 52]. This diagram is like the phase diagrams of atomic systems: it presents gaslike and liquid-like areas together with a critical point. The present samples are chemically prepared to be either in the gaslike or in the fluid-like states. Former non-polarized SANS measurements have confirmed the structure of the present solutions [20, 21, 25], allowing a precise localization of their respective states in the diagram (figure 1 and table 1). Those SANS measurements also show that the characteristic spatial range of the repulsive interparticle potential is here of the order of 20–90 Å [25].

3.3. Magnetic properties

At room temperature, maghaemite and cobalt ferrite are ferrimagnetic materials. The nanoparticles are magnetic monodomains (neglecting here their surface magnetism). They bear a permanent magnetic moment $\vec{\mu}$, the nanoparticle spin, of modulus $\mu = m_S \frac{\pi d^3}{6}$. d is the magnetic diameter of the nanoparticle and m_S the magnetization of the material

Table 1. Characteristics of the colloidal solutions. Φ : volume fraction of nanoparticles as determined by chemical titration; $\Delta\ell_N^2$: nanoparticle/solvent nuclear contrast; $\Delta\ell_M^2$: nanoparticle/solvent magnetic contrast; γ : parameter of dipolar interaction inside the colloidal solution; $\chi_{anapol}(\Phi)$: initial magnetic susceptibility as measured by neutron polarization analysis.

Sample	Φ (%)	Solvent	Nanoparticle material	$\Delta\ell_N^2$ (cm ⁻⁴)	$\Delta\ell_M^2$ (cm ⁻⁴) ^b	γ	$\chi_{anapol}(\Phi)$
A	A0 3.4	D ₂ O	CoFe ₂ O ₄	4×10^{18} ^a	1.01×10^{20}	0.41	0.13
	A1 1.0	H ₂ O				0.12	—
	A2 4.3	H ₂ O	CoFe ₂ O ₄	4.53×10^{21}	1.01×10^{20}	0.52	—
	A3 9.9	H ₂ O				1.20	0.35
B	B1 0.7					0.29	—
	B2 3.3	H ₂ O	CoFe ₂ O ₄	4.53×10^{21}	1.01×10^{20}	1.39	0.51
	B3 9.4					3.95	1.9
	B4 19					8.00	5.92
C	C1 0.5	H ₂ O	γ -Fe ₂ O ₃	5.67×10^{21}	7.95×10^{19}	0.04	—
	C2 11					0.99	—
	D1 0.4					0.05	—
D	D2 2.4	H ₂ O	γ -Fe ₂ O ₃	5.67×10^{21}	7.95×10^{19}	0.34	—
	D3 9					1.26	0.46
E	E1 0.5	H ₂ O	γ -Fe ₂ O ₃	5.67×10^{21}	7.95×10^{19}	0.12	—
	E2 5.6					1.34	0.47

^a In that case the contribution to the nuclear scattering of the citrate coating of the nanoparticles cannot be forgotten—see text.

^b $\Delta\ell_M^2$ is here calculated using the bulk m_S value (4.22×10^5 A m⁻¹ for CoFe₂O₄ and 3.75×10^5 A m⁻¹ for γ -Fe₂O₃).

which constitutes the nanoparticles. It is taken here equal to its bulk value at 300 K $m_S = 3.75 \times 10^5$ A m⁻¹ for γ -Fe₂O₃ and 4.22×10^5 A m⁻¹ for CoFe₂O₄. The magnetic moment of the nanoparticles is of the order of 10^4 Bohr magnetons. Thanks to the rotational degrees of freedom of the nanoparticles in the liquid carrier, the resulting medium behaves, under an applied field H , like a giant paramagnetic material.

3.3.1. Under-field behaviour of the magnetization M . In the dilute regime where the interparticle interaction is negligible (volume fraction $\leq 1\%$), the magnetization curve $M(H)$ can be described by a Langevin formalism:

$$M = m_S \Phi L(\xi) \quad \text{with } L(\xi) = \coth(\xi) - \xi^{-1} \text{ and } \xi = \mu_0 \frac{\mu H}{kT} \quad (1)$$

$L(\xi)$ being the Langevin function and ξ the Langevin argument with μ_0 the vacuum permeability. The maximum value of M is $M_{sat} = m_S \Phi$. In a first approximation we assimilate the magnetic volume fraction to the one determined by chemical titration. The Langevin argument ξ is particle size dependent, and assuming a log-normal distribution of diameters $P(d) = \frac{1}{(2\pi)^{1/2} \sigma d} \exp(-\frac{1}{2\sigma^2} \ln^2(\frac{d}{d_0}))$, $M(H)$ measurements can be adjusted to determine a mean-magnetic size $d_0 = \exp(\langle \ln d \rangle)$ and a standard deviation σ . Figure 2 gives an example of $M(H)/M_{sat}$ variations for sample D2 in the dilute regime and its adjustment to equation (1). Table 2 gives d_0 and σ for all our samples.

In the concentrated regime, in order to take into account the magnetic inter-particle interaction under the applied field we use, in a mean field approximation, an effective field model, and the magnetization is then written [15]

$$M = m_S \Phi L(\xi_e) \quad (2)$$

Table 2. Characteristics of the nanoparticles; d_0 : mean magnetic diameter ($\ln d_0 = \langle \ln d \rangle$) as deduced from the adjustment of the magnetization curve by a Langevin formalism weighted by a log-normal distribution of particle diameters; σ : standard deviation of the log-normal distribution of magnetic diameters; $\frac{\gamma}{\Phi}$: reduced parameter of dipolar interaction, characteristic of the nanoparticles and independent of the volume fraction; R_g^M : magnetic radius of gyration of the nanoparticles as deduced from the magnetic scattering of neutrons; R_g^N : nuclear radius of gyration of the nanoparticles as deduced from the non-polarized experiment; V_w : weight averaged volume of the nanoparticles as deduced from the non-polarized experiment.

Sample	d_0 (nm)	σ	$\frac{\gamma}{\Phi}$	R_g^M (nm)	R_g^N (nm)	V_w (nm ³)
A	7.8	0.2	12	3.7	4.9	6.2×10^2
B	9.5	0.3	42	5.5	8.1	1.4×10^3
C	7.1	0.15	9	—	3.4	3.0×10^2
D	8.5	0.15	14	4.1	5.1	7.3×10^2
E	9.5	0.2	24	4.7	7.0	1.1×10^3

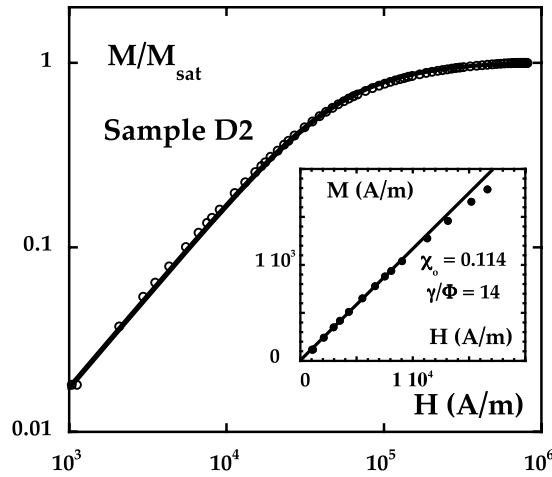


Figure 2. Reduced magnetization curve $M(H)/M_{sat}$ of sample D2 in a log-log representation. The full curve is the fit of $M(H)/M_{sat}$ by a Langevin function weighted by a log-normal distribution (fit parameters: $d_0 = 8.5$ nm and $\sigma = 0.15$). Inset: $M(H)$ in low fields. The initial susceptibility χ is the slope of the full line; here $\Phi = 2.4\%$ and $\chi = \chi_0 = \frac{\gamma}{5} = 0.114$, thus $\gamma = 0.34$ and $\frac{\gamma}{\Phi} = 14$.

with ξ_e given by the self-consistent equation

$$\xi_e = \xi + \lambda\gamma L(\xi_e) \quad (3)$$

where λ is the effective field constant and γ the dipolar interaction parameter (see below). If the effective field constant is null, we recover equation (1) without interparticle interaction. The classical Lorentz value of λ is 0.33. In [25–27], keeping the effective field constant as a free parameter (as proposed in [53] for example), an effective value of λ of 0.22 has been found for MF solutions. Several alternative descriptions of the magnetization in the concentrated regime exist. Let us quote the second order perturbation model of [54] or the mean spherical model of [55]. Note that all these three descriptions merge together in low field for $\gamma \leq 5.5$ (see figure 3).

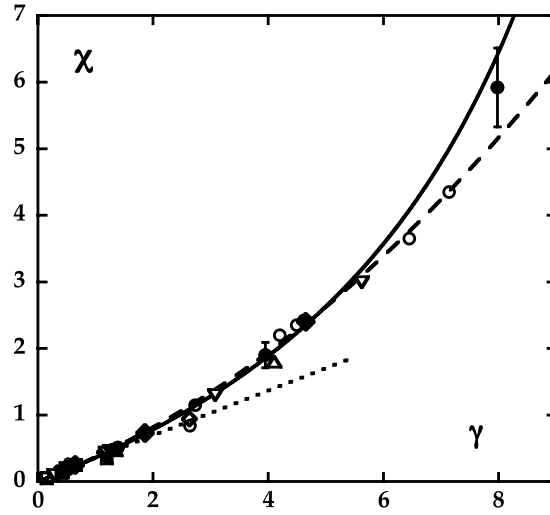


Figure 3. Initial susceptibility χ as a function of the parameter γ of magnetic dipolar interaction for various colloidal solutions (at various Φ and for various nanoparticle characteristics either based on γ - Fe_2O_3 or on CoFe_2O_4). *Open symbols:* χ is determined by magnetization measurements as in the inset of figure 2; (\square) sample A; (\circ) sample B; (\triangle), (\diamond), (∇) and (\blacklozenge) respective samples of [26, 56, 57] and [58]. *Full symbols:* $\chi = \chi_{\text{anapol}}$ is determined by the neutron polarization analysis; (\blacksquare) sample A; (\bullet) sample B; (\blacktriangledown) sample D and (\blacktriangle) sample E. The full curve corresponds to equation (6) with $\lambda = 0.22$, the dotted line to equation (5), $\chi_0 = \gamma/3$, and the dashed curve to the second order perturbation model of [54] (see the text).

3.3.2. Magnetic susceptibility χ . The initial susceptibility χ is related to the dipolar interactions, characterized by the parameter γ which is written $\gamma = \mu_0\mu^2/r^3kT$ where r is the mean interparticle distance. This parameter γ is the ratio of the energy of dipolar interaction to the thermal energy, for two aligned dipoles. It can be written as

$$\gamma = \mu_0 m_s^2 \frac{\pi d^3 \Phi}{6 kT}. \quad (4)$$

Thus in the whole range of concentrations γ is proportional to Φ . The quantity $\frac{\gamma}{\Phi}$ is a constant characteristic of the nanoparticles and independent of the volume fraction. $\frac{\gamma}{\Phi}$ can be determined from initial susceptibility measurements at low volume fraction (see the inset of figure 2).

Indeed at low volume fractions ($\Phi \ll 1$) $\xi_e \approx \xi$ and γ is simply related to χ_0 through the Langevin expression (1). It is written

$$\chi_0 = \lim_{\xi \approx \xi_e \ll 1} (M/H) \approx \Phi m_s \frac{\mu_0 \mu}{3kT} = \frac{\gamma}{3} \quad \text{for } \Phi \ll 1. \quad (5)$$

As for $\xi = \xi_e \ll 1$, χ_0 is proportional to Φ , it is easy to determine the constant $\frac{\gamma}{\Phi} = \frac{3\chi_0}{\Phi}$. Table 2 gives $\frac{\gamma}{\Phi}$ for each sample from a χ_0 measurement at low Φ . Taking into account the characteristics of the magnetic nanoparticles and the Φ -range of the solutions investigated here, γ ranges from 0.04 up to ≈ 8 (see table 1).

At any volume fractions Φ (and by definition of χ in the limit $\xi \ll 1$) equation (3) leads to

$$\chi(\Phi) = \frac{\frac{\gamma}{3}}{1 - \frac{\lambda\gamma}{3}}. \quad (6)$$

Figure 3 plots direct initial susceptibility $\chi(\Phi)$ measurements as a function of parameter γ for different samples either from table 2 at various Φ or from [26, 56–58]. Note that in [58], the

γ/Φ value is very large (=100 as deduced from the χ_0 plot of figure 1 of [58]). It is shown in the simulation work of [59] that at large γ/Φ , χ presents a subsidiary dependence on γ/Φ for $\gamma > 6$. We thus only plot in figure 3 the experimental values of [58] associated with $\gamma \leq 6$. The experiments are compared to expression (6) using $\lambda = 0.22$ and also to the second order perturbation model of [54]: $\chi = \frac{\gamma}{3}(1 + \lambda\frac{\gamma}{3} + \frac{1}{144}(\frac{\gamma}{3})^2)$ with $\lambda = 1/3$ valid for $\Phi < 18\%$ (and which differ in our range of γ by less than 4% from the mean spherical model of [55]). These direct χ measurements will be also compared in next section with the determinations deduced from polarization analysis of magnetic SANS intensity.

4. Static nuclear and magnetic SANS

4.1. Theoretical background

A non-magnetized MF can be considered as a paramagnet, since the orientations of the magnetic monodomain nanoparticles are isotropically distributed. The interaction between a nucleus and a neutron has a magnetic as well as a nuclear contribution. They lead to non-interfering contributions (incoherent) as well as interferences between the waves scattered by each nucleus (coherent scattering).

4.1.1. Non-polarized SANS (zero field). For a non-polarized sample, we can separate the measured scattering cross section into three contributions:

$$\left(\frac{d\sigma(q)}{d\Omega}\right)_{nonPol} = \left(\frac{d\sigma}{d\Omega}\right)_{Inc} + \left(\frac{d\sigma}{d\Omega}\right)_N + \left(\frac{d\sigma}{d\Omega}\right)_M. \quad (7)$$

\vec{q} is the scattering wavevector defined as $\vec{q} = \vec{k}_i - \vec{k}_f$ where \vec{k}_i and \vec{k}_f are respectively the incoming and the scattered wavevectors. The subscripts *Inc*, *N* and *M* stand respectively for incoherent, coherent nuclear and coherent magnetic cross sections; The subscript *non Pol* stands for non-polarized.

Coherent nuclear scattering. Under zero magnetic field, a magnetic fluid will always rearrange such that the scattering is isotropic. The *coherent nuclear cross section* is written

$$\left(\frac{d\sigma}{d\Omega}\right)_N = I_N = \Delta\ell_N^2 n V_w^2 F_N(q) S_N(q, \Phi). \quad (8)$$

$\Delta\ell_N^2$ is the squared difference of nuclear scattering length densities (therefore the unit is cm^{-4}) between the nanoparticles and the solvent carrier (see table 1)—we neglect in this simple presentation the contribution of the citrate coating of the nanoparticles. Note that its contribution can become important, at low $\Delta\ell_N^2$ values in D_2O solvent for example (see further on in part 4.3.1). n is the number of scattering objects per unit volume and V_w is their weight average nuclear volume. We take $\Phi = nV_w \cdot F_N(q)$ as the nuclear form factor of the nanoparticles and $S_N(q, \Phi)$ as the nuclear structure factor of the solution.

In the limit of low volume fractions, $S_N(q, \Phi) \approx 1$ and the I_N measurements allow a determination of the nuclear form factor $F_N(q)$. For isolated spherical particles, it can be written in the low q limit as

$$F_N(q) \approx \exp\left(-\frac{1}{3}(qR_g^N)^2\right) \quad \text{if } qR_g^N \leq 1 \quad (9)$$

where R_g^N corresponds to the spatial distribution of mass of the nanoparticles, which we will call here the ‘nuclear radius of gyration’.

At larger volume fractions, the nuclear structure factor $S_N(q, \Phi)$ departs from unity and it is possible to determine it from the experiment [20, 25]. $S_N(q, \Phi)$ expresses the structure of the colloid, that is the spatial distribution of the centres of mass of the nanoparticles under their mutual interactions. In the $q = 0$ limit, it is proportional to the osmotic compressibility of the solution. The interaction parameter K_T^o , proportional to A_2 , the second virial coefficient of the osmotic pressure ($K_T^o = 2\rho^2 A_2 V_w N_a \rho$ being the mass density of the particles and N_a the Avogadro number) [21, 25], can be easily determined from a plot of $\frac{\Phi}{I_N(q=0, \Phi \rightarrow 0)}$ as a function of Φ as

$$S_N(q = 0, \Phi)^{-1} = \Delta \ell_N^2 V_w \frac{\Phi}{I_N(q = 0, \Phi \rightarrow 0)} \approx 1 + K_T^o \Phi. \quad (10)$$

An experimental plot of $\frac{\Phi}{I_N(q=0, \Phi \rightarrow 0)}$ as a function of Φ allows determination of both V_w and the parameter K_T^o which characterizes the thermodynamic interactions of the solution. Experimentally K_T^o is positive if repulsion is dominant [21, 25]. Close to the liquid–gas transition, in a narrow range of states, it may be found experimentally to be weakly negative [21]. Depending on the strength of the repulsion, K_T^o may either be temperature independent [19] or on the contrary strongly temperature dependent [21, 22]. This contribution can be sensitive to a magnetic field only via the magnetic contribution to the global thermodynamic interaction between the nanoparticles. Under an applied field, the nuclear structure factor $S_N(q, \Phi)$ and the interaction parameter K_T may become anisotropic [25].

Incoherent scattering. This contribution I_{Inc} comes from non-correlated fluctuations of the nuclei of each species (at different positions) in their length of diffusion, nuclear I_{IncN} (different isotopes) as well as magnetic I_{IncM} (degenerated states). The strongest incoherent scattering cross sections are due to H nuclei (80 barns) and D nuclei (2 barns). In our case this (mainly) corresponds to light and heavy water, i.e. the solvents. Incoherent scattering is almost flat in q .

Magnetic scattering. In the range of magnetic fields and temperature studied here, correlated orientations of nuclear spins are not met in the solvent. They are only linked with the magnetic orientation of the spin of the nanoparticles. In zero magnetic field, the magnetic cross section of that paramagnetic material can always be written

$$\left(\frac{d\sigma}{d\Omega} \right)_M = I_M = \Delta \ell_M^2 n V_M^2 F_M(q) S_M(q, \Phi) \quad (11)$$

where $\Delta \ell_M^2 = \frac{2}{3} \left(\frac{r_e}{g} \mu_{neut} \frac{m_S}{\mu_B} \right)^2$ [21–24] is the magnetic contrast (see table 1) with r_e ($=2.818 \times 10^{-15}$ m) the classical radius of the electron, μ_{neut} ($= -1.913$ nuclear magneton units) the magnetic moment of the neutron, m_S has been defined as the material magnetization of the nanoparticles (see section 3), g ($=2$) the Landé factor and μ_B ($=9.27 \times 10^{-24}$ J T $^{-1}$) the Bohr magneton. By analogy with nuclear scattering, V_M is called the magnetic volume of the nanoparticles, $F_M(q)$ their magnetic form factor and $S_M(q, \Phi)$ the magnetic structure factor of the solution.

As for nuclear scattering, the magnetic scattering in the low interaction regime allows us to determine the magnetic form factor $F_M(q)$. For isolated spherical particles, it can be written in the low q limit as

$$F_M(q) \approx \exp\left(-\frac{1}{3}(q R_g^M)^2\right) \quad \text{if } q R_g^M \leq 1 \quad (12)$$

where R_g^M will be the magnetic radius of gyration of the nanoparticles.

The measurement of the magnetic cross section I_M at $q = 0$ is an (initial) magnetic susceptibility determination. In other words, we can rewrite equation (11) in the limit $q = 0$

using equations (4) and (5):

$$I_M(q=0, \Phi) = \left(\frac{r_e \mu_{neut}}{g \mu_B} \right)^2 \frac{2kT}{\mu_0} \chi_0 S_M(q=0, \Phi) = \left(\frac{r_e \mu_{neut}}{g \mu_B} \right)^2 \frac{2kT}{\mu_0} \chi(\Phi) = 5.4 \chi(\Phi) \quad \text{in cm}^{-1} \quad \text{(at room temperature)} \quad (13)$$

assimilating $\chi_0 S_M(q=0, \Phi)$ to $\chi(\Phi)$. Using equations (5), (6) and (13) we find

$$S_M^{-1}(q=0, \Phi) = \left(\frac{r_e \mu_{neut}}{g \mu_B} \right)^2 \frac{2kT}{3\mu_0} \frac{\gamma}{\Phi} \frac{\Phi}{I_M(q=0, \Phi)} = \frac{\chi_0}{\chi(\Phi)} = 1 - \frac{\lambda\gamma}{3}. \quad (14)$$

In order to compare such SANS measurements to direct magnetization determinations, here also it is convenient to plot $\frac{\Phi}{I_M(q=0, \Phi \rightarrow 0)}$ as a function of Φ . Using equation (14), this leads to

$$\frac{\Phi}{I_M(q=0, \Phi \rightarrow 0)} = 0.55 \frac{\Phi}{\gamma} (1 + K_M \Phi) \quad \text{(in cm}^{-1}) \quad (15)$$

with $K_M = -\frac{\lambda\gamma}{3\Phi}$. This magnetic interaction parameter is negative, as on average the magnetic dipolar interaction is attractive. The determination of $\frac{\Phi}{I_M(q=0, \Phi \rightarrow 0)}$ at $\Phi = 0$ gives the value of the parameter $\frac{\gamma}{\Phi}$ for the particles and the determination of the slope of the plot gives the parameter K_M which appears here as the magnetic analogue of the thermodynamic parameter K_T^o .

Under an applied field, the magnetic contribution I_M can become anisotropic for two reasons. First, the magnetic form factor $F_M(q)$ becomes anisotropic under the individual orientation of the nanoparticle spin (see [45] for example). Second, the magnetic structure factor $S_M(q, \Phi)$ may also become anisotropic under field if it induces anisotropic interparticle magnetic correlations.

SANS determinations of I_N and of I_M are powerful and complementary tools to precisely characterize the colloidal solutions. In particular I_N allows us to reach their global thermodynamic state, while I_M focuses only on the magnetic aspects. This sorts out the magnetic interaction, which can be studied independently in deep detail.

In a standard SANS experiment, the two contributions I_N and I_M are important, together with I_{inc} , that can be determined independently and easily subtracted. The intensity I_M is fully determined by the magnetic characteristic of the colloid. The intensity I_N can be modulated by the choice of the solvent. For example, the nuclear contrast $\Delta\ell_N^2$ of CoFe_2O_4 nanoparticles is modified by a factor of 10^3 whether they are dispersed in H_2O or in D_2O (see table 1). However, with those nanoparticles coated with citrate molecules, there is no pertinent choice of solvent that could completely ‘kill’ the nuclear signal, in order to determine the magnetic signal alone in a standard experiment (see section 4.3.1).

4.1.2. Polarization analysis. A way to determine separately the two contributions I_N and I_M is to take advantage of their different polarization properties. Let us consider now polarized neutrons with an incident polarization vector \vec{P} and look at each contribution of the scattered intensity. The scatterers in the sample have electronic spins $\vec{\mu}$. On an NSE spectrometer, the beam is directed along the Z axis and the scattering vector \vec{q} along the X axis. The incident polarization can be directed along any of the X , Y or Z axes. For each of those three configurations it is possible to measure the intensity associated with the spin-flipped neutrons (those that have reversed their direction by 180°) and that associated with the non-flipped ones. In practice, polarizer and analyser are kept parallel (efficiency of the pair: p). The crossed orientation analysis is performed by introducing a spin flipper (efficiency: f_π) before the analyser, as explained in part 4.2.2 [60].

Table 3. Neutron scattered intensity in the polarized SANS experiment; I_N : coherent nuclear scattered intensity; the incoherent nuclear scattered intensity I_{IncN} is here neglected. I_{IncM} : incoherent magnetic scattered intensity; I_M : magnetic scattered intensity; B_g : electronic background intensity; p : efficiency of the ‘polarizer/analyser’ pair; f_π : efficiency of the π flipper.

Polarization \vec{P}	Neutron spins	π flipper	Scattered intensity
$\parallel X$	Flipped	Off	$(1-p)I_N + pI_M + (p+1)I_{IncM}/3 + B_g$
$\parallel X$	Non flipped	On	$pf_\pi I_N + (1-p)(1-f_\pi)I_N + [p(1-f_\pi) + f_\pi(1-p)]I_M + (1+p+f_\pi-2pf_\pi)I_{IncM}/3 + B_g$
$\parallel Y$	Flipped	Off	$(1-p)I_N + I_M/2 + (p+1)I_{IncM}/3 + B_g$
$\parallel Y$	Non flipped	On	$pf_\pi I_N + (1-p)(1-f_\pi)I_N + I_M/2 + (1+p+f_\pi-2pf_\pi)I_{IncM}/3 + B_g$
$\parallel Z$	Flipped	Off	$(1-p)I_N + I_M/2 + (p+1)I_{IncM}/3 + B_g$
$\parallel Z$	Non flipped	On	$pf_\pi I_N + (1-p)(1-f_\pi)I_N + I_M/2 + (1+p+f_\pi-2pf_\pi)I_{IncM}/3 + B_g$

The *coherent nuclear scattering* (which leads to a coherent contribution I_N and an incoherent one I_{IncN} , here negligible) does not modify the polarization of neutrons.

The *incoherent magnetic scattering* (which leads to I_{IncM} , the second contribution to I_{Inc}) changes the polarization of neutrons. Those scattered neutrons have a polarization $\vec{P}_{inc} = -\frac{\vec{P}}{3}$ (2/3 ‘spin flip’ and 1/3 ‘non-spin-flip’).

The *magnetic neutron scattering* (which leads to I_M) obeys two rules. First, only the components of the scatterer spin $\vec{\mu}$ which are perpendicular to the scattering vector \vec{q} , contribute to the cross-section. Second, during the interaction between the spin \vec{s} of the neutron and the spin $\vec{\mu}$ of the scatterers,

- \vec{s} keeps its polarization if \vec{s} is parallel to $\vec{\mu}$ (‘non-spin-flip’ scattering) and
- \vec{s} is flipped if \vec{s} is perpendicular to $\vec{\mu}$ (‘spin flip’ scattering).

As \vec{q} is parallel to X , in the NSE geometry whatever the neutron polarization it is only the projection of $\vec{\mu}$ in the plane YZ which contributes to the scattered intensity I_M . As an example, let us suppose that the neutron spins are polarized along X . Both the Y component of the magnetic moment μ_Y , leading to $I_M/2$, and the Z component μ_Z , leading to $I_M/2$, are perpendicular to the neutron spin and thus flip its direction. Hence the magnetic part of the scattering intensity is pI_M if the spin flipper is off and $[p(1-f_\pi) + f_\pi(1-p)]I_M$ if the spin flipper is on.

The scattered intensity in the various possible configurations is given in table 3 [60], B_g being the electronic background intensity. I_{IncM} and B_g are experimentally determined. The experimental characteristics p and f_π are known. It is then possible to obtain separately the two contributions I_N and I_M , which is not possible from a non-polarized experiment.

4.2. Static experiments

4.2.1. Static non-polarized SANS experiments. The scattering experiments are performed in the Laboratoire Léon Brillouin (LLB) Saclay, on the PAXE and PAXY spectrometer of the LLB (CEA-CNRS) at the reactor Orphée (CE-Saclay, France). The neutron wavelength is $\lambda_n = 10 \text{ \AA}$ and the detector distance is 3.2 m, leading to a scattering vector q ranging from 0.008 to 0.07 \AA^{-1} . A second configuration is also used ($\lambda_n = 5 \text{ \AA}$ with a detector distance of 1.05 m, leading to a scattering vector q ranging from 0.06 to 0.13 \AA^{-1}). The fluid dispersion is introduced between two quartz discs separated by an annular spacer, the thickness of which lies

between 0.1 and 1 mm, depending on the volume fraction of particles. The intensity I_{nonPol} (see equation (7)) of the scattered neutrons is recorded on a planar bi-dimensional detector and regrouped as a function of the scattering vector \vec{q} . The experiment is performed either under zero field or under a 680 kA m^{-1} magnetic field, applied in the plane of the sample cell (i.e. perpendicular to the neutron flux). A data treatment is applied in order to subtract the scattering from the solvent and the quartz cell. In all the figures in zero field the error bar on the scattered intensity is smaller than the symbols.

The respective scattering length densities of H_2O , CoFe_2O_4 , D_2O and $\gamma\text{-Fe}_2\text{O}_3$ are $-0.53 \times 10^{10} \text{ cm}^{-2}$, $+6.2 \times 10^{10} \text{ cm}^{-2}$, $+6.4 \times 10^{10} \text{ cm}^{-2}$ and $+7 \times 10^{10} \text{ cm}^{-2}$. Table 1 gives the resulting contrast between the nanoparticles and their solvent.

4.2.2. Static polarized SANS experiments. The polarized SANS experiments are performed with the NSE spectrometer MESS of the LLB in CE-Saclay-France, in its configuration for polarization analysis. The beam is directed along the Z axis. The neutron wavelength is $\lambda_n = 6 \text{ \AA} \pm 16\%$. The monodetector is monitored on an arm turning around a vertical axis. Thus the scattering vector \vec{q} is along the X horizontal axis. Angles lying between 1° and 3° are studied here leading to a q modulus ranging from 0.018 to 0.055 \AA^{-1} . A super-mirror (\vec{P} along Z) polarizes the neutrons longitudinally. A small current is applied in the precession coils (one being put before the sample and the second one after it) to generate a guide field parallel to Z in order to maintain the Z polarization all along the guides. Around the sample, an arrangement of three pairs of Helmholtz coils is used for the polarization analysis to create a field \vec{H}_{pol} directed along X , Y or Z depending on the measurement. \vec{H}_{pol} polarizes the neutrons in its direction during the scattering process. The amplitude of this polarizing field \vec{H}_{pol} is 640 A m^{-1} . Even if it is enough to polarize the neutrons, it is not sufficient to magnetize the MF in an appreciable way. The MF still can be regarded as an isotropic scatterer.

After the second precession coil and before the detector, the analyser (a second super-mirror), which is crossed with the initial polarizer, intercepts the scattered neutrons. Thus in that configuration, only the neutron spins which have been *flipped* before the detector are detected.

The neutron polarization can also be flipped artificially by using a spin flipper consisting of a Mezei π -coil placed as near as possible to the scattering sample. Thus if the flipper π is on, only the neutrons which are *not flipped* by the sample are detected.

Performing measurements in all possible configurations of the polarizing field \vec{H}_{pol} and of the spin flipper, and using table 3, it is possible to determine I_N and I_M at each q , for each sample. The electronic background B_g and the incoherent magnetic contribution of water I_{IncM} are determined experimentally ($I_{IncM}(\text{D}_2\text{O}) = 0$). The efficiency of the polarizer/analyser pair and that of the spin flipper are respectively $p = 0.932$ and $f_\pi = 0.883$.

The calibration of $I_N + I_M$ is given by the intensity I_{nonPol} from the non-polarized experiment. It has been checked experimentally that the samples do not depolarize the neutron beam.

4.3. Experimental results and discussion

4.3.1. Comparison between I_N and I_M . Let us first compare the results obtained with colloidal solutions containing the same nanoparticles and differing by the nature of their solvent. In samples A3 and A4 (4.3 and 9.95%) the nanoparticles are dispersed in light water while in sample A0 (3.4%) they are dispersed in heavy water. We thus modify the nuclear contrast $\Delta\ell_N^2$ by a large factor (see table 1), and thus also the coherent nuclear intensity, while the magnetic contributions remains comparable. For these three samples, figure 4(a) presents $I_{nonPol} = I_N + I_M$ (the incoherent nuclear intensity and the background being already

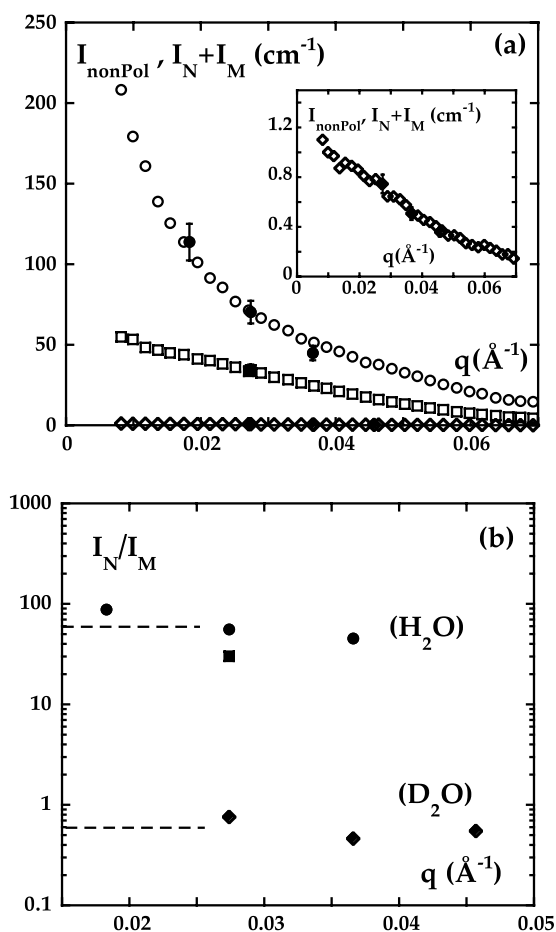


Figure 4. Comparison of I_N , I_M and I_{nonpol} for samples A. (a) q dependence of I_{nonpol} and $I_N + I_M$. Symbols: (\diamond, \blacklozenge) I_{nonpol} and $I_N + I_M$ for sample A0, (\square, \blacksquare) I_{nonpol} and $I_N + I_M$ for sample A2; (\circ, \bullet) I_{nonpol} and $I_N + I_M$ for sample A3. Inset: enlargement for sample A0 in D_2O . (b) Ratio of $\frac{I_N}{I_M}$ as a function of q . In light water it ranges from 30 to 90 while in D_2O it is of the order of 0.6. Symbols: (\blacklozenge) sample A0, (\blacksquare) sample A2 and (\bullet) sample A3. Dashed lines are guides for the eye.

subtracted) as obtained with the non-polarized device and as deduced from the polarization analysis. Let us point out that the q dependence of I_{nonPol} is fairly compatible with those of $I_N + I_M$. This can be seen in figure 4(a) and also in the following figures 5 and 6.

The ratios I_N/I_M obtained for those samples are plotted in figure 4(b). The first important conclusion is that if with the D_2O carrier the intensities I_M and I_N are comparable; in contrast with the H_2O carrier $I_N \gg I_M$. For all the samples with H_2O as solvent, I_M is found experimentally to be at most of the order of a few per cent of I_N (see figure 5). In fact this can be easily predicted by evaluating the ratio $\frac{\Delta\ell_N^2}{\Delta\ell_M^2}$ in H_2O . For cobalt ferrite in H_2O , it is found that $\frac{\Delta\ell_N^2}{\Delta\ell_M^2} = 45$ while experimentally the ratio $\frac{I_N}{I_M}$, which is also sensitive to the form and structure factors, ranges from 30 to 90 for A2 and A3 samples. Thus a non-polarized experiment on samples with ferrite nanoparticles dispersed in light water essentially measures the nuclear contribution of those particles: $I_{\text{nonPol}}(\text{H}_2\text{O}) \approx I_N$ and $I_M \ll I_N$.

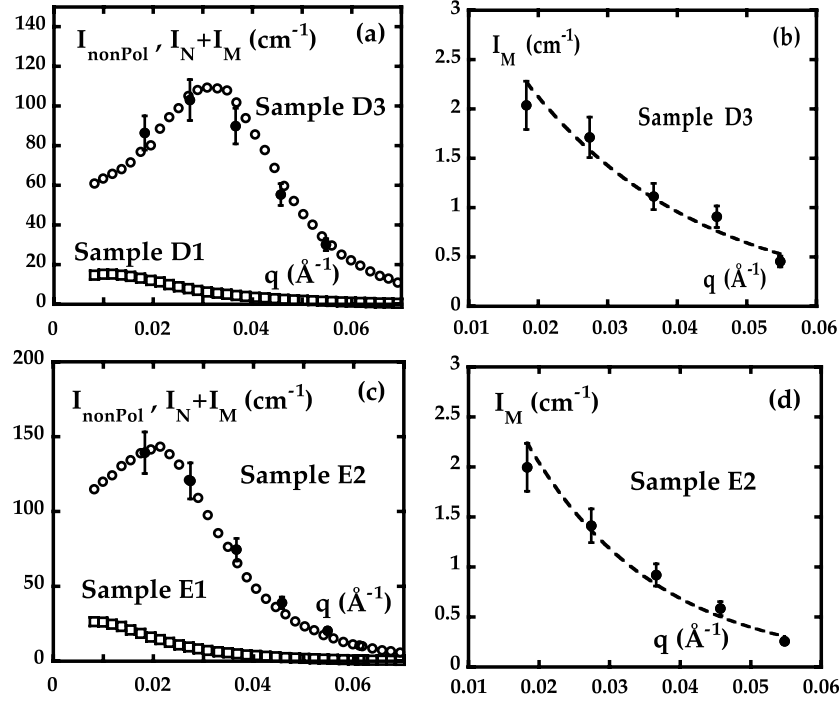


Figure 5. q dependence of the scattered intensity of samples D and E as obtained in the polarized and non-polarized SANS experiments. (a) Comparison of I_{nonpol} and $I_N + I_M$ for samples D. Symbols: (\square) I_{nonpol} of sample D1, (\circ) I_{nonpol} of sample D3, (\bullet) $I_N + I_M$ of sample D3. (b) Magnetic scattered intensity I_M as a function of the scattering vector q for sample D3. The dashed curve is a guide for the eye. (c) Comparison of I_{nonpol} and $I_N + I_M$ for samples E. Symbols: (\square) I_{nonpol} of sample E1, (\circ) I_{nonpol} of sample E2, (\bullet) $I_N + I_M$ of sample E2. (d) Magnetic scattered intensity I_M as a function of the scattering vector q for sample E2. The dashed curve is a guide for the eye.

In contrast, evaluating $\frac{\Delta\ell_N^2}{\Delta\ell_M^2}$ in D_2O one finds 0.04 for CoFe_2O_4 nanoparticles. The experimental ratio is found to be $\frac{I_N}{I_M} \approx 0.6$ for the A0 sample, which is still small, but 15 times more than the calculation. This discrepancy has to be ascribed to the citrate coating of the nanoparticles. If D_2O is the solvent and because of the respective values of the scattering length densities of citrate, CoFe_2O_4 , D_2O and $\gamma\text{-Fe}_2\text{O}_3$, the contribution of the citrate shell increases I_N for CoFe_2O_4 nanoparticles while it makes I_N decrease for $\gamma\text{-Fe}_2\text{O}_3$ nanoparticles. This shell contribution is not easy to calculate as the density of citrate inside the shell as well as its thickness are not precisely known. Note that for samples containing ferrite nanoparticles dispersed in H_2O , this shell contribution only becomes important while evaluating the nuclear form factor of the particles at large q , in the so-called Porod regime [61].

In conclusion, playing with the nature of the solvent in which the particles are dispersed, it is not possible to determine the magnetic contribution alone with a non-polarized experiment. The polarization analysis is thus necessary to determine I_M . In contrast, if the nanoparticles are dispersed in H_2O , the nuclear contribution largely dominates the magnetic one and we obtain

$$I_M \ll I_N \quad \text{and} \quad I_{\text{nonPol}} = I_N + I_M \approx I_N.$$

Hereafter, we only present experiments with nanoparticles dispersed in H_2O for which $I_{\text{nonPol}} \approx I_N$.

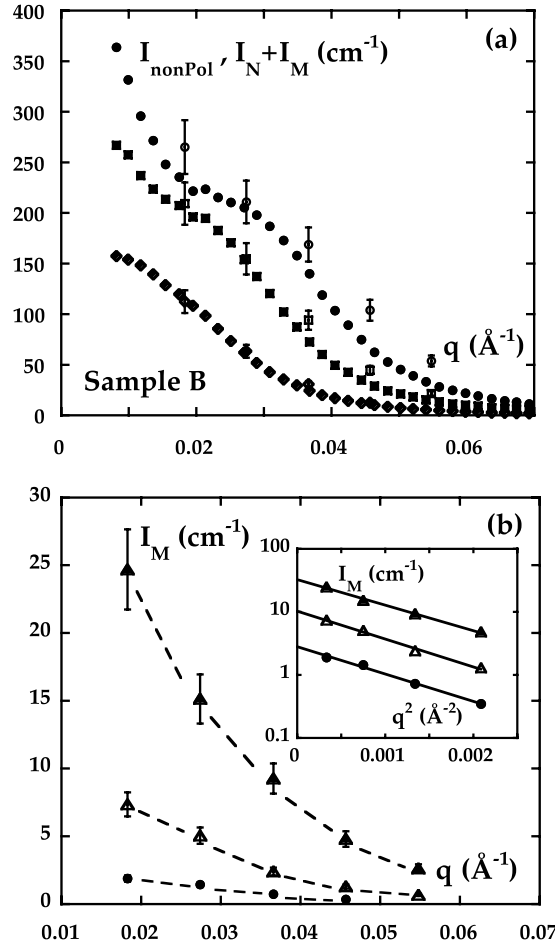


Figure 6. q dependence of the scattered intensity of sample B at various Φ as obtained in the polarized and non-polarized SANS experiments. (a) Comparison of I_{nonpol} and $I_N + I_M$. Symbols: (\blacklozenge , \blacklozenge) I_{nonpol} and $I_N + I_M$ for sample B2, (\blacksquare , \square) I_{nonpol} and $I_N + I_M$ for sample B3, (\bullet , \circ) I_{nonpol} and $I_N + I_M$ for sample B4. (b) Magnetic scattered intensity I_M as a function of the scattering vector q . Symbols: (\bullet) sample B2, (Δ) sample B3 and (\blacktriangle) sample B4. Inset: semi-logarithmic plots of I_M as a function of q^2 for samples B2, B3 and B4. The full lines are exponential fits of $I_M(q^2)$; the value at $q = 0$ leads to the determination of $\chi_{\text{anapol}}(\Phi)$ of table 1 through $I_M(q = 0, \Phi) = 5.4\chi_{\text{anapol}}(\Phi)$.

4.3.2. Interparticle interaction coefficients. Figures 5 and 6 compare I_{nonPol} and I_M , obtained for various samples, with nanoparticles dispersed in H_2O . As in figure 4(a), it is clear that $I_N + I_M$ nicely reproduces the q dependence of I_{nonPol} whatever its shape or order of magnitude. Figures 5 and 6 also clearly illustrate the fact that I_N ($\approx I_{\text{nonPol}}$) and I_M probe very different structures in the same colloidal solution. At a given concentration I_N may present a peak of correlation while I_M does not.

Moreover we can study the Φ dependence of the scattered intensity (extrapolated at $q = 0$ —see expressions (10) and (15)). Separating nuclear and magnetic scattering allows isolation of magnetic interactions from the other contributions. Indeed, nuclear scattering is sensitive to all the thermodynamic interparticle interactions inside the solution, namely

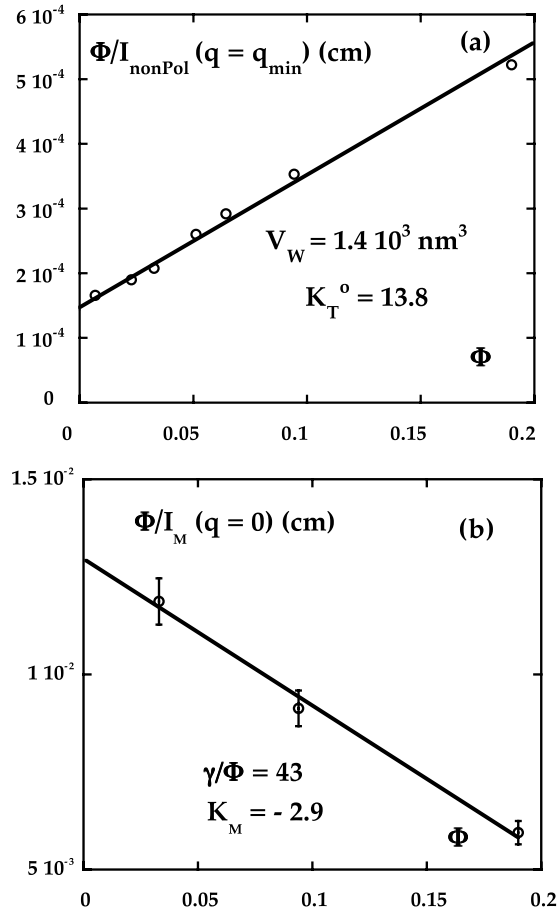


Figure 7. Comparative plots of the Φ dependence of $\frac{\Phi}{I_{nonPol}} (\approx \frac{\Phi}{I_N})$ and of $\frac{\Phi}{I_M}$ at $q \approx 0$ for sample B (fluid carrier H_2O). (a) Plot of $\frac{\Phi}{I_{nonPol}} (\approx \frac{\Phi}{I_N})$ at $q = q_{min} = 7 \times 10^{-3} \text{ \AA}^{-1}$ as a function of Φ (see equation (10)). The full line corresponds to $V_W = 1.4 \times 10^3 \text{ nm}^3$ and $K_T^o = 13.8$. (b) Plot of $\frac{\Phi}{I_M}$ extrapolated at $q = 0$ (see the inset of figure 6 (b)) as a function of Φ . The full line is a fit to equation (15). It leads to $\frac{\gamma}{\Phi} = 43$ and $K_M = -2.9$.

here van der Waals, magnetic dipolar, electrostatic and eventually steric [20]. In contrast the magnetic scattering is only sensitive to the magnetic dipolar interaction and is able to sort it out from the other ones.

In order to check quantitatively the interparticle interactions, measurements have been performed with solutions of the same nanoparticles dispersed in H_2O at different volume fractions. Figure 6 presents the Φ dependence of I_{nonPol} and I_M for samples B2, B3 and B4 ($\Phi = 3.3, 9.4$ and 19%). From those data, we can extract $\frac{\Phi}{I(q=0)}$ and plot it versus Φ , for both the nuclear and the magnetic contributions. For the nuclear contribution we assimilate $I_{nonPol}(q = q_{min} = 7 \times 10^{-3} \text{ \AA}^{-1})$ to $I_{nonPol}(q \approx 0)$, as in [25]. For the magnetic contribution, an extrapolation to $q = 0$ is performed using equation (12) (see the inset of figure 6(b)). Figure 7 compares the Φ dependence of $\frac{\Phi}{I_{nonPol}(q=7 \times 10^{-3} \text{ \AA}^{-1})}$ and $\frac{\Phi}{I_M(q=0)}$. Figure 7(a), which has already been presented in [25], presents results obtained at different concentrations for our present sample B (called sample A in [25]).

The first comment is that the interparticle interactions have opposite influences on $\frac{\Phi}{I_{nonPol}(q \approx 0)}$ and on $\frac{\Phi}{I_M(q=0)}$. Figure 7(a) presents an increasing linear behaviour of $\frac{\Phi}{I_{nonPol}(q \approx 0)}$ with Φ , associated with $V_w = 1.44 \times 10^3 \text{ nm}^3$ and $K_T^o = 13.8$ (see equation (10) and [25]). It reflects a repulsive global interaction which is expected in this ‘fluid-like’ phase (see figure 1). In contrast figure 7(b) reflects a magnetic interparticle interaction which is attractive. It is also natural. Dipolar interaction is anisotropic; however, its mean field average in zero field is attractive. Let us quantify it. In figure 7(b) $\frac{\Phi}{I_M(q=0)}$ appears as an increasing function of Φ which can be adjusted to equation (14) with $\frac{\gamma}{\Phi} = 43$ and $K_M = -2.9$. If it is natural to observe a magnetic attraction between the nanoparticles, however, we have noted before that this attraction is far from being dominant among the whole set of interparticle interactions. The second virial coefficient of the osmotic pressure being positive ($K_T^o \approx 13.8$), repulsion is the leading contribution (in particular $K_T^o \approx 13.8$ contains the negative dipolar contribution $K_M = -2.9$). It confers its stability to the fluid phase. This fact explains why in such colloidal conditions we do not observe any chaining of the nanoparticles in zero field [25].

Let us now compare I_M , the measured magnetic contribution to SANS, to direct magnetization measurements performed at the macroscopic scale. The values of $\frac{\gamma}{\Phi}$ and K_M can also be determined from direct magnetization measurements. For sample B, this leads to $\frac{\gamma}{\Phi} = 42$ (table 2) and $K_M = -3.1$ (using equations (13) and (15)), values which are in very good agreement with those determined above from the scattering experiment $\frac{\gamma}{\Phi} = 43$ and $K_M = -2.9$ (figure 7(b)).

From our measurements on the other samples such an extrapolation of $\frac{\Phi}{I_M(q=0)}$ to $\Phi = 0$ is unfortunately not possible. However for each sample, at a given volume fraction, an extrapolation to $q = 0$ can be performed using equation (12) leading to $I_M(q = 0, \Phi)$. Equation (13) then gives a straightforward deduction of the magnetic susceptibility $\chi_{anapol}(\Phi)$ of each colloidal solution. The obtained $\chi_{anapol}(\Phi)$ values are all reported in table 1 and compared to direct $\chi(\Phi)$ measurements in figure 3. The agreement between the two kinds of measurement is rather good at any Φ . Moreover the experimental measurements also agree rather well both with our model for describing the magnetic interaction in the MF (equation (6)) and with the second order perturbation model of [54] (which is only valid for $\Phi < 18\%$).

4.3.3. Determination of nuclear and magnetic sizes of the nanoparticles. In the limit $\Phi = 0$, the structure factor S_M (respectively S_N) tends towards 1 and $(\frac{I_M}{\Phi})_{\Phi=0}$ (respectively $(\frac{I_N}{\Phi})_{\Phi=0} \approx (\frac{I_{nonPol}}{\Phi})_{\Phi=0}$ for samples in light water) reduces to $\Delta \ell_M^2 V_M F_M(q)$ (respectively $\Delta \ell_N^2 V_W F_N(q)$). Guinier plots of $(\frac{I_M}{\Phi})_{\Phi=0}$ and $(\frac{I_{nonPol}}{\Phi})_{\Phi=0}$ allow the determination of R_g^M and R_g^N using equations (9) and (12). Figures 8(a) and (b) present such semi-log representations as a function of q^2 for sample B. Table 2 collects those size determinations for all the present samples. Taking into account the low $\frac{\gamma}{\Phi}$ value of samples D (respectively E), R_g^M has been deduced at $\Phi = 8\%$ (respectively 5.6%). For the less polydisperse samples, the magnetic radius of gyration compares well to the magnetic radius $\frac{d_M}{2}$ deduced from the magnetization curves. R_g^M is always smaller than R_g^N , on average by a factor ≈ 0.7 . This difference has to be addressed to a magnetic small grain effect. The nanoparticles have an external layer of disordered spins, of typical thickness 1 nm, which does not contribute to the magnetic scattering in the present experiment [30]. It reduces the magnetic radius of gyration with respect to the nuclear one.

4.3.4. Nuclear and magnetic structure factors. The nuclear and the magnetic structure factors are deduced from the measurements at various Φ by a standard procedure (see [20, 21, 25]):

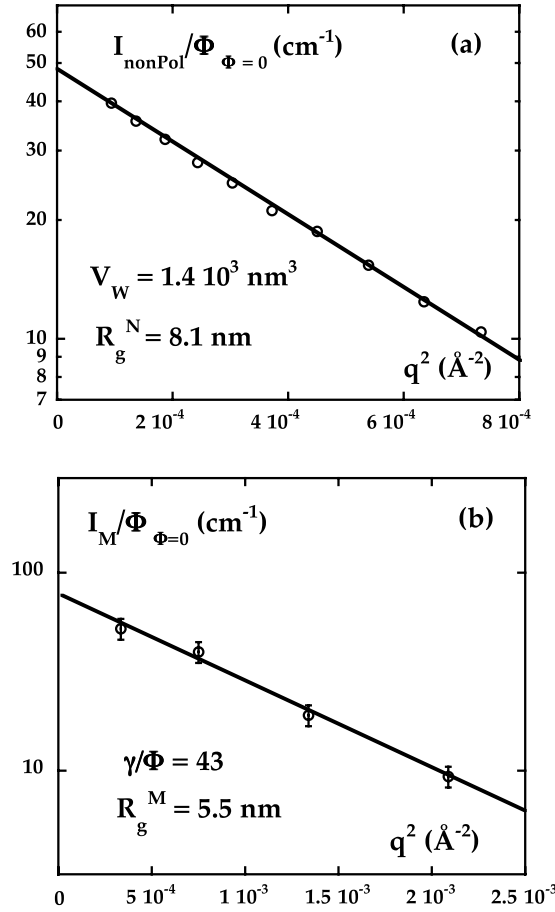


Figure 8. Nuclear and magnetic Guinier plots for sample B. (a) Semi-logarithmic representation of $\frac{I_{\text{nonPol}}}{\Phi}$ ($\approx \frac{I_N}{\Phi}$) extrapolated at $\Phi = 0$, as a function of q^2 . The full line is a fit to equations (8) and (9). It corresponds to $V_W = 1.4 \times 10^3 \text{ nm}^3$ and $R_g^N = 8.1 \text{ nm}$. (b) Semi-logarithmic representation of $\frac{I_M}{\Phi}$ extrapolated at $\Phi = 0$ as a function of q^2 . The full line is a fit to equations (11) and (12). It corresponds to $\frac{\gamma}{\Phi} = 43$ and $R_g^M = 5.5 \text{ nm}$.

$$S_N(q, \Phi) = \frac{\left(\frac{I_N(q, \Phi)}{\Phi}\right)}{\left(\frac{I_N(q, \Phi)}{\Phi}\right)_{\Phi=0}} \quad \text{and} \quad S_M(q, \Phi) = \frac{\left(\frac{I_M(q, \Phi)}{\Phi}\right)}{\left(\frac{I_M(q, \Phi)}{\Phi}\right)_{\Phi=0}}.$$

The results for sample B are presented in figure 9. $S_N(q, \Phi)$ and $S_M(q, \Phi)$ have quite different behaviours. At large concentrations $S_N(q, \Phi)$ presents a (smooth) maximum associated with the correlation peak of the first neighbours. In contrast, $S_M(q, \Phi)$ is, within the experimental accuracy, independent of q . It is always larger than unity and $S_M(q, \Phi) \approx S_M(q = 0, \Phi)$ (see the inset of figure 9). The correlation of spin orientation is independent of the probed spatial scale for these samples in the fluid phase. They behave as paramagnetic materials.

At this stage, we could raise an apparent contradiction between the nuclear and the magnetic structure factors. The magnetic scattering at a vector q , as well as the nuclear one, occurs when two neutrons hit two nanoparticles separated by a distance $r \sim 1/q$. If the nuclear scattering is low at this given q , this means that there are few pairs of particles separated by such a distance. Therefore this should be seen as well for the magnetic scattering.

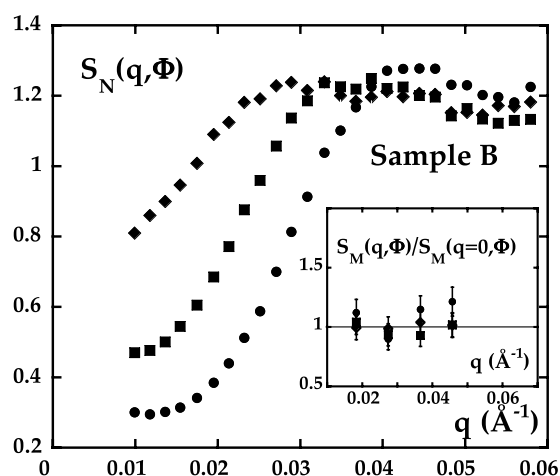


Figure 9. Nuclear structure factor S_N of sample B at various Φ as a function of q . Inset: reduced representation of the magnetic structure factor $\frac{\chi_0 S_M(q, \Phi)}{\chi(\Phi)} = \frac{S_M(q, \Phi)}{S_M(q=0, \Phi)}$ at various Φ as a function of q . Symbols: (◆) sample B2, (■) sample B3 and (●) sample B4.

However the magnetic scattering is linked with the spin orientation correlation between two scatterers. Since our solutions are paramagnetic, there are no orientation correlations between the macrospins of two different nanoparticles, hence no correlation between the spins of two nuclei pertaining to two different particles. So the magnetic signal loses any information about the spatial interparticle correlations.

4.3.5. Under-field behaviour of the nuclear contribution. One of the main properties of the dipolar magnetic interaction is that it is anisotropic. An important consequence of this anisotropy can be a chaining of the nanoparticles in zero field. Recent observations agree with a chaining [62] with ionic MF if the superficial density of charge of the nanoparticles is low [63]. However in the present samples, the electrostatic repulsion is rather strong and this chaining does not occur. The anisotropy of the magnetic interaction is then difficult to evidence in zero magnetic field as the magnetic moments are oriented at random. However an applied field removes this orientational degeneracy, as it orientates the magnetic moments of the nanoparticles along its own direction. An under-field SANS measurement is in principle able to evidence this anisotropy of interaction. This is however difficult in an I_M determination (polarized SANS under field) because this effect is only of the second order. Indeed I_M is already anisotropic under field because of the orientation of the magnetic moments itself, even if they are not interacting together. In contrast, in an I_N determination (polarized SANS under field or non-polarized SANS under field in light water) this effect is the only possible origin of anisotropy (if the nanoparticles are spherical).

Such experiments, investigating the SANS under-field behaviour of ionic MF in the fluid phase of figure 1, have been performed in [25] with a non-polarized device. In those under-field studies it was therefore necessary to separate I_M from I_N . In practice we have just seen that for samples in light water the I_N contribution is much larger than I_M . Knowing that, we can be sure that our measurements under field indeed reveal the anisotropy of spatial correlation induced by the field. The main conclusions of that under-field investigation were the observation of

- an anisotropic scattering at low q related to a strong anisotropy of osmotic compressibility

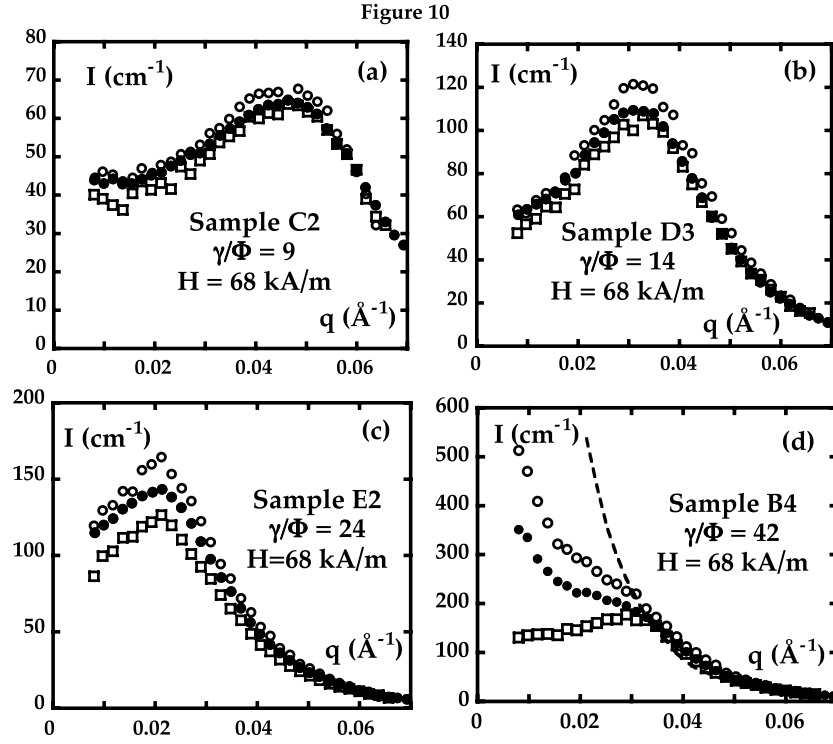


Figure 10. Comparison for various samples between the scattered intensity $I_{nonPol}(q, H=0) \approx I_N^{H=0}(q)$ obtained with the non-polarized experiment at $H=0$ averaged on rings at constant q (symbol \bullet) and the anisotropic intensities at $H=68 \text{ kA m}^{-1}$ averaged on a sector of $\pm 15^\circ$ along the field direction (I_N^\parallel , symbol \square) and perpendicular to the field direction (I_N^\perp , symbol \circ). (a) Sample C2, $\frac{\gamma}{\Phi} = 9$; (b) sample D3, $\frac{\gamma}{\Phi} = 14$; (c) sample E2, $\frac{\gamma}{\Phi} = 24$; (d) sample B4, $\frac{\gamma}{\Phi} = 42$. The dashed curve corresponds to $0.19\Delta\ell_N^2 V_w F_N(q)$; it is the intensity that would be expected for non-interacting particles. At small q it is larger than I_N^\parallel , I_N^\perp and $I_N^{H=0}$: there is no agglomeration of the particles under a field.

(this is due to the macroscopic demagnetizing effect associated with the magnetic interparticle interaction) and

- at larger q an anisotropy of concentration fluctuations with a lowering of those fluctuations along the applied field, associated with a gaslike structure in that direction. This observation is incompatible with a contact chaining of the nanoparticles under field in those colloidal conditions.

We present here results obtained for the various samples of table 1 at a given field 680 kA m^{-1} and at the largest volume fraction available. Figure 10 presents the under-field anisotropy of non-polarized scattered intensity for samples C2, D3, E2 and B4 (here $I_{nonPol} \approx I_N$). I_N^\parallel (respectively I_N^\perp) is the scattered intensity over a sector of $\pm 15^\circ$ around the direction parallel (respectively normal) to the applied field. One method of characterizing this anisotropy at $q \rightarrow 0$ was introduced in [25]; namely,

$$\begin{aligned} \left(\frac{\beta_\lambda}{\Phi}\right)_{\text{exp}} &= \frac{1}{\Phi} \left(\frac{1}{S_N^\parallel(q=0, \Phi)} - \frac{1}{S_N^\perp(q=0, \Phi)} \right) \\ &= \Delta\ell_N^2 V_w \left(\frac{1}{I_N^\parallel(q=0, \Phi)} - \frac{1}{I_N^\perp(q=0, \Phi)} \right) \end{aligned} \quad (16)$$

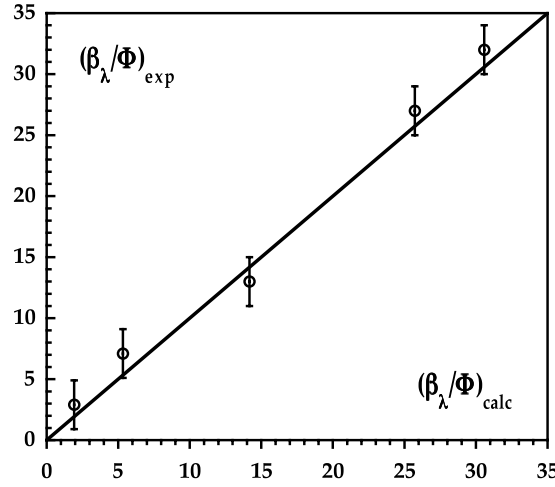


Figure 11. Correlation between $(\frac{\beta_\lambda}{\Phi})_{exp}$ obtained experimentally at $H = 68 \text{ kA m}^{-1}$ using equation (16) and $(\frac{\beta_\lambda}{\Phi})_{calc}$ obtained from equation (17) with the sample characteristics (tables 1 and 2) and the help of equations (1), (2) and (3). *From top to bottom: sample B4, sample of [56], sample E2, sample D3 and sample C2.*

where S_N^{\parallel} (respectively S_N^{\perp}) is the structure factor in the direction parallel (respectively normal) to the applied field.

This anisotropy associated with a demagnetizing effect is related to fluctuations of macroscopic field inside the solution. It has been modeled in [25] as

$$\left(\frac{\beta_\lambda}{\Phi}\right)_{calc} = \frac{\frac{\gamma}{\Phi} L^2(\xi_e)}{[1 - \lambda\gamma L'(\xi_e)][1 + (1 - \lambda)\gamma L'(\xi_e)]} \quad (17)$$

by using the same basic model for the magnetic interaction as presented here in part 3.3. Figure 11 compares $(\frac{\beta_\lambda}{\Phi})_{exp}$ to $(\frac{\beta_\lambda}{\Phi})_{calc}$ for various samples of very different $\frac{\gamma}{\Phi}$ values. A good correlation is found as $\frac{\gamma}{\Phi}$ varies from 9 to 42.

This shows that the same simple magnetic model (part 3.3) is able to quantify both

- the magnetic interparticle interaction as measured by magnetic scattering in zero field and
- the anisotropic contribution to the global interparticle interaction coming from the macroscopic demagnetizing effect as measured by under-field nuclear scattering.

5. Quasi-elastic small angle neutron scattering

5.1. Theoretical background

A quasi-elastic experiment allows us to reach the temporal dependence of the intensity scattered by the solution. Two kinds of dynamic can be probed in an NSE experiment:

- magnetic dynamics, that of the magnetic moment, eventually inside the nanoparticle crystal itself,
- nuclear dynamics, the Brownian dynamic of the whole nanocrystal.

Here we are only concerned with this second kind of dynamics, as we are always dealing with nanoparticles dispersed in light water. In that case we have seen that the nuclear signal is, on average, two orders of magnitude larger than the magnetic one. Our quasi-elastic

measurements thus reflect a nuclear dynamic associated with the motion of the nanoparticles inside the suspension in presence of the other particles. With respect to the static measurements, the specificity of this dynamic experiment is that it is sensitive to hydrodynamic interaction. Indeed, here, the hydrodynamic interaction also becomes relevant in addition to all the interparticle interactions of importance in the static experiment.

In a spin-echo measurement, it is the intermediate scattering function, $S(q, \Phi, t)$, which is determined. In an experiment where the nuclear scattering is dominant, we find

$$\frac{I_N(q, \Phi, t)}{I_N(q, \Phi, t = 0)} = \frac{S_N(q, \Phi, t)}{S_N(q, \Phi, t = 0)} \quad (18)$$

$S_N(q, \Phi, t = 0)$ being the static nuclear structure factor. The experimental decay of $S_N(q, t)$ can be adjusted to a simple exponential relaxation:

$$S_N(q, \Phi, t) = S_N(q, \Phi, t = 0) \exp\left(-\frac{t}{\tau(q, \Phi)}\right). \quad (19)$$

This characteristic time $\tau(q, \Phi)$ is associated with the relaxation of concentration fluctuations of wavelength $\frac{2\pi}{q}$. One can relate it to an effective diffusion coefficient $D(q, \Phi)$ which can be defined by

$$\tau^{-1}(q, \Phi) = D(q, \Phi)q^2. \quad (20)$$

For non-interacting particles in a solvent at room temperature, $D(q, \Phi)$ reduces to a classical Brownian diffusion coefficient:

$$D_0 = \frac{kT}{f_0} = \frac{kT}{6\pi\eta_0 R_H} \quad (21)$$

f_0 being the friction coefficient at infinite dilution, η_0 being the solvent viscosity and R_H the hydrodynamic radius of the nanoparticles.

For interacting particles, one can always write

$$D(q, \Phi) = D_0 \frac{H(q, \Phi)}{S_N(q, \Phi, t = 0)} \quad (22)$$

which defines the hydrodynamic function $H(q, \Phi)$. $H(q, \Phi)$ accounts for the q and Φ dependence of $D(q, \Phi)$ under the hydrodynamic interaction and $S_N(q, \Phi)$ for the q and Φ dependence of $D(q, \Phi)$ under the thermodynamic interactions. Note that $H(q, \Phi)$, which describes the indirect coupling of the particles via the suspending fluid, also depends on all the thermodynamic interactions (via the many-particle correlations).

In the limit $q = 0$, the diffusion process concerns large scale particle motions, over distances large compared to their own radius. $D(q, \Phi)$ then can be identified with the collective diffusion coefficient of the generalized Stokes–Einstein equation [64, 65]. Such a limit is reached for example in a Rayleigh forced scattering experiment [26, 27] probing collective mass diffusion at a spatial scale of 10–100 μm and at a timescale of the order of 1 s. $H^{-1}(q = 0, \Phi \rightarrow 0)$ can be seen as a reduced collective friction coefficient that can be developed at low Φ as

$$H^{-1}(q = 0, \Phi \rightarrow 0) = \frac{f(\Phi \rightarrow 0)}{f_0} \approx 1 + K_f \Phi \quad (23)$$

$f(\Phi)$ being the friction coefficient at volume fraction Φ and K_f an hydrodynamic interaction coefficient. For hard spheres, it is found that $K_f = 6.55$ [66].

Using the development at $q = 0$ and low Φ of the structure factor (equation (10)), the effective diffusion coefficient (equation (22)) is written in that limit:

$$D(q = 0, \Phi \rightarrow 0) \approx D_0(1 + (K_T - K_f)\Phi). \quad (24)$$

At intermediate q , $S_N(q, \Phi)$ is responsible for the now well known slowing down of the diffusion around the first peak (at $q = q_{max}$) of strongly structured suspensions [38–42, 67]. It is often referred to as the ‘cage effect’. For its part, the behaviour of $H(q, \Phi)$ in that q range is still an open question. In [41, 42] it is found experimentally to go through a maximum slightly larger than unity at $q R_g^N \approx 2$. In contrast in [38–40] this maximum is found to be always smaller than unity.

For large q , $S_N(q, \Phi) \rightarrow 1$ and the nanoparticles experience a self-diffusion process if the probed spatial scale $2\pi/q$ is smaller than the mean interparticle distance at the volume fraction Φ , that is if $q > q_{max}$ (in the present repulsive fluid phases). In that limit, the effective diffusion coefficient is written

$$D(q \rightarrow \infty, \Phi) = D_0 H(q \rightarrow \infty, \Phi). \quad (25)$$

For uncharged hard spheres and in the limit of small Φ , one theoretically expects from virial expansion [59, 68, 69]

$$H(q \rightarrow \infty, \Phi \rightarrow 0) = 1 - 1.73\Phi. \quad (26)$$

That is $H(q \rightarrow \infty, \Phi = 10\%) = 0.83$ and $H(q \rightarrow \infty, \Phi = 20\%) = 0.67$ for hard spheres. A smaller concentration dependence is found by numerical simulations for charged spheres by [70].

The whole theoretical description of the hydrodynamical function is not easy. It involves many-body processes. A renormalization method has been proposed for hard spheres by [69–71]. $H(q)$ is found to have a pronounced q dependence with oscillations recalling those of the structure factor (see [40, 64, 69, 71]). It is found to be always smaller than unity. Hydrodynamic interaction then seems to behave as an additional friction exerted on the particles which depends on the local structure.

Another method has been proposed for strongly interacting charged particles by [72, 73] under the assumption that indirect hydrodynamic interactions can be considered as pairwise additive (as assumed in expressions (23), (24) and (26)). This description is thus restricted to low volume fractions and low to moderate salinity. The maximum of $H(q)$ is found to be larger than unity. It is concentration and ionic strength dependent. $H(q)$ also presents here oscillations as a function of q reminding those of the structure factor (see [40, 72, 73]). By opposition to [69, 71] it thus predicts a speeding-up of the dynamics on length scales comparable to the interparticle distance for those strongly interacting charged colloids.

NSE here probes spatial scales ranging from 50 to 300 Å at timescales of the order of 10 ns. At the largest q , it may probe self-diffusion of effectively single particles. As the smallest q is of the same order of magnitude as q_{max} , the experiment may then explore the ‘cage effect’.

5.2. Neutron spin echo (NSE)

Those dynamical experiments are also performed with the spin echo MESS of the LLB in CE-Saclay-France, now in its echo configuration. The beam is directed along the Z axis. The neutron wavelength is $\lambda_n = 6 \text{ \AA} \pm 16\%$. Angles lying between 1.5° and 7° are studied here, leading to a modulus of the scattering vector \vec{q} (directed along the X axis) ranging from 0.03 to 0.13 \AA^{-1} . With respect to the configuration for polarization analysis, the arrangement of three pairs of Helmholtz coils is suppressed. A flipper $\pi/2$ is added after the polarizer, at the entrance of the first precession coil (C_1 , length L_1 , field H_1). This flipper $\pi/2$ turns the neutron polarization from parallel to Z to perpendicular to Z and thus initiates the Larmor precession of the neutron spins about the field H_1 inside C_1 . A second flipper $\pi/2$ is added at the end of the second precession coil (C_2 , length L_2 , field H_2) before the analyser, in order to turn the polarization back along Z .

Inside the precession coil C_1 (respectively C_2), the neutron spins precess by an angle $\alpha_1 = \frac{\gamma_n H_1 L_1}{v_1}$ (respectively $\alpha_2 = \frac{\gamma_n H_2 L_2}{v_2}$) where γ_n is the gyromagnetic ratio of the neutron, v_1 (respectively v_2) being the incoming (respectively outgoing) velocity of neutrons. Between C_1 and C_2 the flipper π reverses the spin component of the ZX plane, which is equivalent to changing α_1 to $-\alpha_1$.

For quasi-elastic scattering, the condition $L_1 H_1 = L_2 H_2$ must be satisfied. The energy transfer $\hbar\omega = \frac{1}{2} M_n (v_2^2 - v_1^2)$ may be deduced (at the first order in ω) from the final precession angle $\alpha = \alpha_1 - \alpha_2 = \omega t$, where $t = \frac{\hbar \gamma_n H_1 L_1}{M_n v_1^3}$ is the precession duration and M_n the neutron mass. The detected signal $P_{NSE}(t)$ (*NSE* standing for neutron spin echo), after the second $\pi/2$ flipper and the analyser, is proportional to $\langle \cos \alpha \rangle$. It is related to the scattering function $S(q, \omega)$ by

$$P_{NSE}(t) = P_S \langle \cos \alpha(t) \rangle = P_S \frac{\int S(q, \omega) \cos(\omega t) d\omega}{\int S(q, \omega) d\omega}. \quad (27)$$

P_S takes into account the eventual change of the neutron polarization by the scattering process itself. For nuclear scattering, $P_S = 1$ and

$$P_{NSE}(t) = \frac{S_N(q, t)}{S_N(q, t=0)}. \quad (28)$$

In practice, the spectrometer has been calibrated by measuring the NSE signal for a standard graphite sample (which is an elastic scatterer with $P_S = 1$), giving the instrumental resolution function.

5.3. Dynamical experimental results and discussion

Figure 12 presents the experimental relaxation of P_{NSE} for sample D3 at $\Phi = 9\%$ and $q = 7.3 \times 10^{-2} \text{ \AA}^{-1}$. The signal, already calibrated by the instrument resolution function, is adjusted to an exponential relaxation of characteristic time $\tau(q = 7.3 \times 10^{-2} \text{ \AA}^{-1}, \Phi = 9\%) = 64.5 \text{ ns}$ (cf expression (19)). By using expression (20) an effective diffusion coefficient $D(q = 7.3 \times 10^{-2} \text{ \AA}^{-1}, \Phi = 9\%) = 2.9 \times 10^{-11} \text{ m}^2 \text{ s}^{-1}$ can be deduced. The q and Φ dependence of the effective diffusion coefficient is presented in the inset of figure 12 for samples D2 and D3. The values of the non-interacting diffusion coefficient D_0 are obtained from equation (21) with the assumption that for those colloids $R_H \approx R_g^N$ as found by light scattering for silica particles in [41] for example. Respectively for samples A, B and D it is found that $D_0 = 4.33 \times 10^{-11}$, 2.62×10^{-11} and $4.16 \times 10^{-11} \text{ m}^2 \text{ s}^{-1}$.

We probe here the hydrodynamic interaction in the high q range ($1.7 \leq q R_g^N \leq 10.4$) where only scarce measurements are available (they cover the range $0.5 \leq q R_g^N \leq 3.5$ for charge-stabilized colloidal silica [30–32]). We deduce the hydrodynamic function $H(q, \Phi)$ from equation (22), $S(q, \Phi)$ being extrapolated to unity for $q > 7 \times 10^{-2} \text{ \AA}^{-1}$ if no measurement is available. $H(q, \Phi)$ is plotted in figure 13 as a function of $q R_g^N$ for various samples (A, B and D) and various Φ .

For a comparison the value of the hydrodynamic function $H(q \approx 10^{-5} \text{ \AA}^{-1}, \Phi = 10\%) = 0.56$ deduced from the Rayleigh forced scattering experiment of [40] (obtained with a sample based on $\gamma\text{-Fe}_2\text{O}_3$ nanoparticles of characteristics similar to those of sample B3) is also plotted in figure 13(b). This value is rather close to the hard sphere limit at $q = 0$ (equation (23)) also plotted on the figures, together with the hard sphere limit at $q \rightarrow +\infty$ (equation (26)). In figures 13(a) at $\Phi \approx 3\%$ and 13(c) at $\Phi = 19\%$, the experimental behaviour obtained at $q = 0$ and $q \rightarrow +\infty$ is compatible with hard sphere values. However a smooth intermediate maximum of the order of 1.2 is observed at $q R_g^N \approx 2.2$. Those observations are also true for

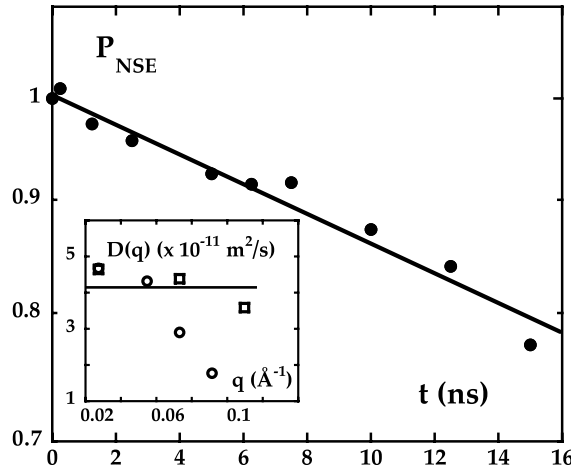


Figure 12. Relaxation of the spin-echo signal P_{NSE} as a function of time for sample D3 at $q = 7.3 \times 10^{-2} \text{ \AA}^{-1}$. The full line is a fit to equation (19) using equation (28) with $\tau(q) = 64.5 \text{ ns}$. It leads to an effective diffusion coefficient $D(q = 7.3 \times 10^{-2} \text{ \AA}^{-1}, \Phi = 9\%) = 2.9 \times 10^{-11} \text{ m}^2 \text{ s}^{-1}$. Inset: effective diffusion coefficient as a function of q for samples D2 (\square) and D3 (\circ). The full horizontal line marks the value of the diffusion coefficient for non-interacting nanoparticles $D_0 = 4.16 \times 10^{-11} \text{ m}^2 \text{ s}^{-1}$.

sample B3 in figure 13(b) at $\Phi \approx 10\%$. In contrast, for samples A3 and D3, $H(q, \Phi \approx 10\%)$ strongly decreases from ≈ 1.1 at $qR_g^N \approx 3$ down to ≈ 0.4 at $qR_g^N \approx 4$. The main difference between sample B3 and, samples A3 and D3, besides their quite different polydispersity index (see table 2), is illustrated in inset of figure 13(b). It presents the nuclear structure factor $S_N(q)$ of sample D3. There is a pronounced structure peak at $q \approx 4.5 \times 10^{-2} \text{ \AA}^{-1}$ ($qR_g^N \approx 2.2$), much more pronounced than that of sample B3 (see figure 9). The value of $H(qR_g^N \approx 4, \Phi \approx 10\%)$ for samples A3 and D3 then appears as a not yet damped oscillation of the hydrodynamic function (q being not large enough). In [41], a similar observation on charged colloidal silica was modeled with the help of [69, 71] introducing in the calculation the experimentally deduced interparticle potential (see figure 9 in [41]).

Let us note that from $qR_g^N = 2.2$ up to 3.5, the present experimental behaviour is roughly compatible with the observations of [41] and [42]. In particular, as observed in [41, 42] (and in contrast to [38–40]), $H(q, \Phi)$ is found to be larger than unity in the neighbourhood of the maximum of $S_N(q, \Phi)$. Our result seems compatible with the pairwise approximation of [72, 73] for strongly interacting charged spheres. We observe a speeding-up of the dynamics around $qR_g^N = 2$ and the intuitive interpretation of $H(q, \Phi)$ as being only an ‘extra friction’ (which would mean $H(q, \Phi)$ always smaller than unity) does not seem to apply in our charged colloid. Indeed, $H(q, \Phi)$, which expresses the contribution of the hydrodynamic interactions to the ‘local friction’, also contains a contribution from the thermodynamic interactions. Here two experimental points support this:

- the existence of a maximum of $H(q, \Phi)$ at an intermediate q value for all the samples whatever Φ and
- the value of $H(q, \Phi)$ for samples A3 and D3 at $\Phi \approx 10\%$ and $qR_g^N \approx 4$, compatible with a not yet damped oscillation to be related to the colloidal structure.

However, further more systematic measurements of $H(q, \Phi)$ have to be performed to elucidate in more detail its large q dependence.

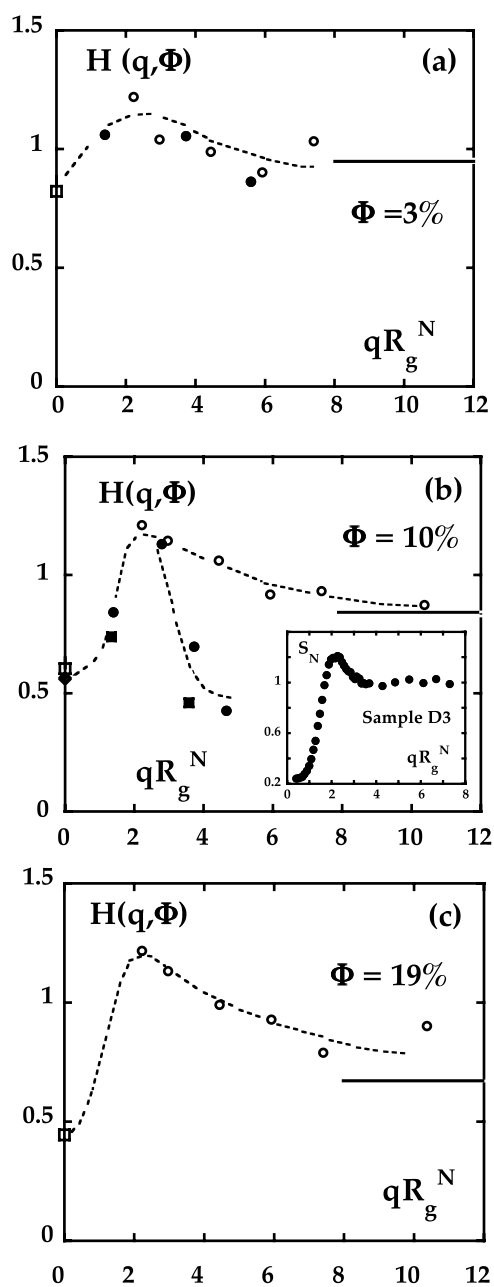


Figure 13. Hydrodynamic function $H(q, \Phi)$ as a function of qR_g^N at various volume fractions. The full lines are the uncharged hard sphere limit at $q \rightarrow \infty$ (equation (26)). The dashed curves are guides for the eye. (a) $\Phi \approx 3\%$; symbols, (O) sample B2, (●) sample D2, (□) Stokes-Einstein limit at $q = 0$ and $\Phi = 3\%$ (equation (24)). (b) $\Phi \approx 10\%$; symbols, (■) sample A3, (O) sample B3, (●) sample D3, (◆) result of the Rayleigh forced scattering experiment of [26, 27], (□) Stokes-Einstein limit at $q = 0$ and $\Phi = 10\%$ (equation (24)). Inset: nuclear structure factor S_N of sample D3 as a function of qR_g^N . (c) $\Phi \approx 19\%$; symbols, (O) sample B4 and (□) Stokes-Einstein limit at $q = 0$ and $\Phi = 19\%$ (equation (24)).

6. Summary and perspectives

We have shown here that the interparticle interaction deeply influences the shape of an MF neutron scattering pattern. The separate analysis of the magnetic and the nuclear contributions to the neutron scattering has demonstrated that they behave differently as functions of q and Φ .

In the fluid phase of our system, the magnetic attractions associated with the magnetic neutron scattering, determined in a polarized SANS experiment, are fairly compatible with direct susceptibility measurements. The magnetic structure factor is independent of the probed spatial scale, while a clear structuring of the colloid can be evidenced by the nuclear structure factor. Indeed, the magnetic attractions are weaker than the global thermodynamic repulsion, deduced from the nuclear neutron scattering. This explains why no contact chaining of the nanoparticles occurs in such ‘repulsive’ samples under the magnetic dipolar interaction.

If the nanoparticles are dispersed in H_2O , the nuclear contribution dominates the non-polarized SANS. Under a magnetic field, the magnetic interparticle interaction becomes anisotropic. In these experimental conditions, if the repulsion is not too strong, an anisotropy of nuclear scattering in low q is observed associated with an anisotropy of compressibility of the MF. This effect is the more pronounced the larger is the parameter of magnetic dipolar interaction. A model of magnetic interaction quantitatively explains together the dependences of the SANS magnetic contribution in zero field, direct magnetic susceptibility measurements and the under-field anisotropy of the SANS nuclear contribution.

Thanks to the crossed analysis of the static and the quasi-elastic nuclear signals, NSE measurements allow determination of the very controversial hydrodynamic function $H(q, \Phi)$. It is found here (in zero field) to be close to that obtained in a pairwise approximation by [72, 73] for strongly interacting charged particles. In particular, as in [41, 42] and contrary to [38–40], it reaches values larger than unity at a spatial scale close to that of the maximum of the nuclear static structure factor. Those preliminary results on MF appeal for a forthcoming more detailed study.

In the future, we plan to explore the structural and dynamical MF properties in other areas of the liquid–gas colloidal phase diagram of the present system [16–18], namely

- the liquid phase, where the thermodynamic interactions are attractive on average, and
- the solid glassy phase, where the dynamics of rotation is seriously hindered as shown by magneto-birefringence relaxation [74]. Such a solid exists both in the range of globally attractive or globally repulsive interparticle interactions [52].

Lots of questions still have to be answered, for example: is it possible to observe an under-field anisotropy of the hydrodynamic function in the vicinity of its maximum, as observed for the diffusion coefficient at $q \approx 0$ in a Rayleigh forced scattering experiment [26, 27]? In strongly concentrated MF systems, is it possible for a magnetic correlation length to exist spontaneously [75, 76]?

Another interesting frame of investigations, out of the scope of the present paper and to be explored in the future, is the local magneto-dynamics of the MF. Several contributions coming from volume [46] and surface [47] magnetic effects inside the nanoparticles enter the game, together with the interparticle interactions. They depend on temperature and nanoparticle characteristics. They make the local magneto-dynamics a whole world to be studied in itself.

Acknowledgments

We thank Sophie Neveu for the chemical synthesis of ferrofluid samples based on CoFe_2O_4 nanoparticles and Annie Brulet for her help in the polarization analysis.

References

- [1] Wilhelm C, Gazeau F and Bacri J-C 2002 *Eur. Biophys. J.* **31** 118
- [2] Wilhelm C, Gazeau F, Roger J, Pons J N and Bacri J-C 2002 *Langmuir* **18** 8148
- [3] Weissleder R, Moore A, Mahmood U, Bhorade R, Benveniste H, Chioocca E A and Basilion J P 2000 *Nat. Med.* **6** 351
- [4] Bulte J W, Douglas T, Witwer B, Zhang S C, Strable E, Lewis B K, Zywicke H, Miller B, van Gelderen P, Moskowitcz B M, Duncan I D and Frank J A 2001 *Nat. Biotechnol.* **19** 1141
- [5] Wilhelm C, Gazeau F, Cebers A and Bacri J-C 2003 at press
- [6] Shliomis M I and Morozov K I 1994 *Phys. Fluids* **6** 2855
- [7] Bacri J-C, Perzynski R, Shliomis M I and Burde G I 1995 *Phys. Rev. Lett.* **75** 2128
- [8] Zahn M and Greer D R 1995 *J. Magn. Magn. Mater.* **149** 165
- [9] Rosensweig R E 1996 *Science* **271** 614
- [10] Embs J P, Muller H W, Wagner C, Knorr K and Lücke M 2000 *Phys. Rev. E* **61** R2196
- [11] Bacri J-C, Cebers A and Perzynski R 1994 *Phys. Rev. Lett.* **72** 2705
- [12] Gazeau F, Heegaard B M, Bacri J-C, Cebers A and Perzynski R 1996 *Phys. Rev. E* **54** 3672
Gazeau F, Heegaard B M, Bacri J-C, Cebers A and Perzynski R 1996 *Europhys. Lett.* **35** 609
- [13] Gazeau F, Baravian C, Bacri J-C, Perzynski R and Shliomis M 1997 *Phys. Rev. E* **56** 614
- [14] Rosensweig R E 1985 *Ferrohydrodynamics* (Cambridge: Cambridge University Press)
- [15] Blums E, Cebers A and Maiorov M M 1997 *Magnetic fluids* (New York: de Gruyter)
- [16] Shliomis M I 1972 *Sov. Phys.-JETP* **31** 1291
- [17] 1996 *Magnetic Fluids and Applications Handbook* ed B Berkovsky (New York: Begell)
- [18] Fauconnier N, Bée A, Roger J and Pons J N 1996 *Prog. Colloid Polym. Sci.* **100** 212
- [19] Dubois E, Cabuil V, Boué F, Bacri J-C and Perzynski R 1997 *Prog. Colloid Polym. Sci.* **104** 173
- [20] Dubois E, Cabuil V, Boué F and Perzynski R 1999 *J. Chem. Phys.* **111** 7147
- [21] Dubois E, Perzynski R, Boué F and Cabuil V 2000 *Langmuir* **16** 5617
- [22] Cousin F, Dubois E and Cabuil V 2001 *J. Chem. Phys.* **115** 6051
- [23] Cousin F 2000 *Thesis* Université Paris 6
- [24] Cousin F, Dubois E and Cabuil V 2003 at press
- [25] Gazeau F, Dubois E, Bacri J-C, Boué F, Cebers A and Perzynski R 2002 *Phys. Rev. E* **65** 031403
- [26] Bacri J-C, Cebers A, Bourdon A, Demouchy G, Heegaard B M, Kashevsky B and Perzynski R 1995 *Phys. Rev. E* **52** 3936
- [27] Bacri J-C, Cebers A, Bourdon A, Demouchy G, Heegaard B M and Perzynski R 1995 *Phys. Rev. Lett.* **74** 5032
- [28] Bacon G E 1962 *Neutron Diffraction, Monographs on the Physics and Chemistry of Materials* ed W Jackson, H Frölich and N F Mott (London: Oxford University Press)
- [29] Hayter J B 1991 *J. Chem. Soc. Faraday Trans.* **87** 403
- [30] Bellouard C, Mirebeau I and Hennion M 1996 *Phys. Rev. B* **53** 5570
- [31] Aksel'rod L A, Gordeev G P, Drabkin G M, Lazebnik I M and Lebedev V T 1986 *Sov. Phys.-JETP* **64** 312
- [32] Wiedenmann A 2000 *J. Appl. Crystallogr.* **33** 428
- [33] Wiedenmann A 2001 *Physica B* **297** 226
- [34] Kammel M, Hoell A and Wiedenmann A 2001 *Scr. Mater.* **44** 2341
- [35] Anthore R, Petipas C, Chandesris D and Martinet A 1977 *J. Physique Coll.* **38** C2 203
- [36] Anthore R, Gauthier S, Martinet A and Petipas C 1980 *IEEE Trans. Magn.* **16** 197
- [37] Lal J, Abernathy D, Auvray L, Diat O and Grübel G 2001 *Eur. Phys. J. E* **4** 263
- [38] Grübel G, Abernathy D L, Riese D O, Vos W L and Wegdam G H 2000 *J. Appl. Crystallogr.* **33** 424
- [39] Riese D O, Wegdam G H, Vos W L, Sprik R, Fenistein D, Bongaerts J H H and Grübel G 2000 *Phys. Rev. Lett.* **85** 5460
- [40] Robert A 2001 *Thesis*, Université Grenoble 1
- [41] Philippe A P and Vrij A 1988 *J. Chem. Phys.* **88** 6459
- [42] Phalakornkul J K, Gast A P, Pecora R, Nägele G, Ferrante A, Mandl-Steininger B and Klein R 1996 *Phys. Rev. E* **54** 661
- [43] Cebula D J, Charles S W and Popplewell J 1983 *J. Physique* **44** 207
- [44] Hayter J B and Pynn R 1982 *Phys. Rev. Lett.* **49** 1103
- [45] Pynn R, Hayter J B and Charles S 1983 *Phys. Rev. Lett.* **51** 710
- [46] Casalta H, Schleger P, Bellouard C, Hennion M, Mirebeau I, Ehlers G, Farago B, Dormann J L, Kelsch M, Linde M and Philipp F 1999 *Phys. Rev. Lett.* **82** 1301
- [47] Gazeau F, Dubois E, Hennion M, Perzynski R and Raikher Yu L 1997 *Europhys. Lett.* **40** 575
- [48] Rosman R, Janssen J J M and Rekveldt M Th 1990 *J. Magn. Magn. Mater.* **85** 97

- [49] Grabcev B, Balasoiu M, Tirziu A, Kuklin A I and Bica D 1999 *J. Magn. Magn. Mater.* **201** 140
- [50] Massart R 1981 *IEEE Trans. Magn.* **17** 1247
Massart R 1979 *French Patent Specification* 79-188-42
Massart R 1982 *US Patent Specification* 4-329-241
- [51] Neveu S, Tourinho F, Bacri J-C and Perzynski R 1993 *Colloids Surf. A* **80** 1
- [52] Cousin F, Dubois E, Cabuil V, Boué F and Perzynski R 2001 *Braz. J. Phys.* **31** 350
- [53] Dikanski Yu I 1982 *Magnetohydrodynamics* **18** 237
- [54] Ivanov A O and Kuznetsova O B 2001 *Phys. Rev.* **64** 041405
- [55] Morozov K I and Lebedev A V 1990 *J. Magn. Magn. Mater.* **85** 51
- [56] Bacri J-C, Boué F, Cabuil V and Perzynski R 1993 *Colloids Surf. A* **80** 11
- [57] des Villettes C H 1991 *DEA Report* Université Paris 6 unpublished
- [58] Pshenichnikov A F 1995 *J. Magn. Magn. Mater.* **145** 319
- [59] Pshenichnikov A F and Mekhonoshin V V 2000 *J. Magn. Magn. Mater.* **213** 357
- [60] Pouget S 1993 *Thesis* Institut National des Sciences Appliquées de Toulouse
- [61] Dubois E 1997 *Thesis* Université Paris 6
- [62] Zhang H and Widom M 1994 *Phys. Rev. E* **49** R3591
- [63] Cousin F, Bée A, Boué F, Dubois E, Ponton A and Perzynski R 2003 at press
- [64] Pusey P N 1985 *Dynamic Light Scattering: Applications of Photon Correlation Spectroscopy* ed R Pecora (New York: Plenum)
- [65] Hansen J P and MacDonald I R 1990 *Theory of Simple Liquids* (London: Academic)
- [66] Batchelor G K 1982 *J. Fluid Mech.* **119** 379
- [67] Hayter J, Janninck G, Brochard-Wyart F and de Gennes P G 1980 *J. Physique Lett.* **41** L-451
- [68] Rallison J M and Hinch F J 1986 *J. Fluid Mech.* **167** 131
- [69] Beenakker C W J and Mazur P 1983 *Physica A* **120** 388
- [70] Snook I and van Megen W 1984 *J. Colloid Interface Sci.* **100** 194
- [71] Beenakker C W J and Mazur P 1984 *Physica A* **126** 349
- [72] Nägele G, Kellerbauer O, Krause R and Klein R 1993 *Phys. Rev. E* **47** 2562
- [73] Nägele G 1996 *Phys. Rep.* **272** 215
- [74] Meriguet G 2001 *DEA Report* Université Paris 6 unpublished
- [75] Groh B and Dietrich S 1996 *Phys. Rev. E* **53** 2509
- [76] Banerjee S and Widom M 2001 *Braz. J. Phys.* **31** 360